The Astrophysical Journal, 693:750–770, 2009 March 1 doi:10.1088/0004-637X/693/1/750

HUBBLE SPACE TELESCOPE MORPHOLOGIES OF $z \sim 2$ DUST OBSCURED GALAXIES. I. POWER-LAW SOURCES

R. S. Bussmann[1], Arjun Dey[2], J. Lotz[2,11], L. Armus[3], K. Brand[4], M. J. I. Brown[5], V. Desai[3], P. Eisenhardt[6], J. Higdon[7], S. Higdon[7], B. T. Jannuzi[2], E. Le Floc'h[8], J. Melbourne[9], B. T. Soifer[4,9], and D. Weedman[10]

[1] Steward Observatory, Department of Astronomy, University of Arizona, 933 N. Cherry Ave., Tucson, AZ 85721, USA; rsbussmann@as.arizona.edu
[2] National Optical Astronomy Observatory, 950 N. Cherry Ave., Tucson, AZ 85719, USA
[3] *Spitzer* Science Center, California Institute of Technology, MS 220-6, Pasadena, CA 91125, USA
[4] Giacconi Fellow, Space Telescope Science Institute, Baltimore, MD 21218, USA
[5] School of Physics, Monash University, Clayton, Victoria 3800, Australia
[6] Jet Propulsion Laboratory, California Institute of Technology, MC 169-327, 4800 Oak Grove Drive, Pasadena, CA 91109, USA
[7] Georgia Southern University, P.O. Box 8031, Statesboro, GA, USA
[8] *Spitzer* Fellow, Institute for Astronomy, University of Hawaii, Honolulu, HI 96822, USA
[9] Caltech Optical Observatories, California Institute of Technology, Pasadena, CA 91125, USA
[10] Astronomy Department, Cornell University, Ithaca, NY 14853, USA
Received 2008 August 29; accepted 2008 November 11; published 2009 March 3

ABSTRACT

We present high-spatial resolution optical and near-infrared imaging obtained using the ACS, WFPC2, and NICMOS cameras aboard the *Hubble Space Telescope* of 31 24 μm bright $z \approx 2$ Dust Obscured Galaxies (DOGs) identified in the Boötes Field of the NOAO Deep Wide-Field Survey. Although this subset of DOGs have mid-IR spectral energy distributions dominated by a power-law component suggestive of an AGN, all but one of the galaxies are spatially extended and not dominated by an unresolved component at rest-frame UV or optical wavelengths. The observed $V - H$ and $I - H$ colors of the extended components are 0.2–3 magnitudes redder than normal star-forming galaxies. All but one have axial ratios >0.3, making it unlikely that DOGs are composed of an edge-on star-forming disk. We model the spatially extended component of the surface brightness distributions of the DOGs with a Sérsic profile and find effective radii of 1–6 kpc. This sample of DOGs is smaller than most submillimeter galaxies (SMGs), but larger than quiescent high-redshift galaxies. Nonparametric measures (Gini and M_{20}) of DOG morphologies suggest that these galaxies are more dynamically relaxed than local ULIRGs. We estimate lower limits to the stellar masses of DOGs based on the rest-frame optical photometry and find that these range from $\sim 10^9$–10^{11} $M_\odot$. If major mergers are the progenitors of DOGs, then these observations suggest that DOGs may represent a postmerger evolutionary stage.

Key words: galaxies: evolution – galaxies: fundamental parameters – galaxies: high-redshift

Online-only material: color figures

1. INTRODUCTION

One of the most important questions concerning the evolution of galaxies is when and how the most massive galaxies formed. It has been known since the analysis of the *InfraRed Astronomical Satellite* (*IRAS*) data that in the local universe the most bolometrically luminous galaxies have their spectral energy distributions (SEDs) dominated by infrared (IR) light (Soifer et al. 1986), suggesting that these systems are highly obscured by dust, which absorbs ultraviolet (UV) and optical light and re-radiates it in the IR. While these ultraluminous IR galaxies (ULIRGs) are rare in the local universe, they become an increasingly important phenomenon at high redshift (e.g., Franceschini et al. 2001; Le Floc'h et al. 2005; Pérez-González et al. 2005).

Following the launch of the *Spitzer Space Telescope*, numerous investigators have identified and studied populations of high-redshift galaxies that are IR bright yet optically faint (Yan et al. 2004; Houck et al. 2005; Weedman et al. 2006b; Fiore et al. 2008; Dey et al. 2008). In particular, Dey et al. (2008) and Fiore et al. (2008) present a simple and economical method for selecting these systems using only *R*-band and 24 μm Multiband Imaging Photometer for *Spitzer* (MIPS; Rieke et al. 2004) data. Dey et al. (2008) employ a color cut of $R - [24] > 14$ (Vega magnitudes; $\approx F_\nu(24\ \mu\mathrm{m})/F_\nu(R) > 1000$) to identify objects they call Dust Obscured Galaxies (DOGs) in the Boötes field of the NOAO Deep Wide-Field Survey (NDWFS;[12] B. T. Jannuzi et al. 2009, in preparation; A. Dey et al. 2009, in preparation).

The broadband photometry, redshift distribution, and number density of the DOGs imply that they are undergoing an extremely luminous, short-lived phase of stellar bulge and nuclear black hole growth and may be the progenitors of the most luminous ($\sim 4L^*$) present-day galaxies. Ground-based photometry from the NDWFS suggests magnitudes of $R \approx 24$–27, $I \approx 24$–26, and $K \approx 17.5$–20.5 for the sample of DOGs with $F_\nu(24\ \mu\mathrm{m}) > 0.3$ mJy. DOGs are relatively rare, with a surface density of ≈ 0.089 arcmin^{-2} for sources with $F_{24} > 0.3$ mJy. Spectroscopic redshifts determined for a subsample of DOGs, using the Deep Imaging Multi-Object Spectrograph (DEIMOS; Faber et al. 2003) and the Low Resolution Imaging Spectrometer (LRIS; Oke et al. 1995) on the telescopes of the W. M. Keck Observatory (43 DOGs), as well as the Infrared Spectrometer (IRS; Houck et al. 2004) on *Spitzer* (43 DOGs) have shown that the DOGs have a redshift distribution centered on $z \approx 2$ with a dispersion of $\sigma_z \approx 0.5$. While DOGs are rare, they are sufficiently luminous that they contribute up to one quarter of

[11] NOAO Leo Goldberg Fellow.

[12] http://www.noao.edu/noaodeep

the total IR luminosity density from all $z \sim 2$ galaxies, and constitute the bulk of ULIRGs at $z \sim 2$ (Dey et al. 2008).

Based on their observed properties, Dey et al. (2008) suggest that DOGs may represent a transition stage between submillimeter galaxies (SMGs) and unobscured quasars or galaxies. Evidence in support of this scenario is that DOGs and SMGs have similar space densities and clustering properties (Brodwin et al. 2008). An important test of this scenario is to study their morphologies with high-spatial resolution imaging. For example, one of the primary motivations for the merger-driven scenario for the formation of ULIRGs is their disturbed structure at optical wavelengths (Sanders et al. 1988a). Studies of numerical simulations of galaxy mergers have suggested that they can produce very red, luminous systems that are highly dust obscured (Jonsson et al. 2006). Recently, Lotz et al. (2008) have applied nonparametric methods of quantifying galaxy morphologies to similar merger simulations and have found that mergers are most easily identified during the first pass and at the final coalescence of their nuclei.

In addition to identifying merger activity, morphological information can constrain the size-scale of the emitting region. Sources with active star formation on several kiloparsec (kpc) scales have larger sizes than objects dominated by an active galactic nucleus (AGN) or a very compact, nuclear starburst. Studies of distant red galaxies (DRGs) have shown a relation between star formation and size at rest-frame optical wavelengths in the sense that quiescent DRGs are all very compact with effective radii ($R_{\rm eff}$) less than 1 kpc, while active DRGs tend to be more extended ($1 < R_{\rm eff} < 10$ kpc; Zirm et al. 2007; Toft et al. 2007). Analysis of SMGs in GOODS-N shows extended emission on scales of 5–15 kpc (Pope et al. 2005). Recent NICMOS imaging of a sample of 33 high-z ULIRGs by Dasyra et al. (2008) has shown these extreme objects (which are similar in their selection criteria to DOGs) to have effective radii in the range ∼1.5–5 kpc. About half of their sample shows signs of interactions, but only two are merging binaries with a luminosity ratio $\leqslant$3:1 (i.e., qualifying as major mergers).

High-spatial resolution imaging of the DOGs is essential to understanding their relation to other galaxy populations as well as their role in galaxy evolution in general. We have begun an effort to obtain high-resolution imaging using laser guide star and natural guide star adaptive optics on the Keck telescopes. These (ongoing) efforts have resulted in high-resolution K-band images of a handful of DOGs found near bright stars (J. Melbourne et al. 2009, in preparation). A complementary method of obtaining deep, high-spatial resolution imaging is with the *Hubble Space Telescope* (*HST*). With the Advanced Camera for Surveys (ACS) and the Wide Field Planetary Camera 2 (WFPC2), we can probe the rest-frame UV emission of the DOGs that is sensitive to the ionizing sources associated with ongoing star formation. Meanwhile, NICMOS data allow the study of the rest-frame optical morphology, which better traces the stellar mass and dust-enshrouded AGN.

In this paper, we present ACS/WFPC2 and NICMOS images of 31 DOGs and analyze their morphologies. The DOGs studied in this paper have spectroscopic redshifts from either *Spitzer*/IRS DEIMOS/LRIS were selected primarily based on their large 24 μm flux densities ($F_{24\,\mu{\rm m}} > 0.8$ mJy), and have power-law SEDs in the mid-IR. In a future paper, we will study a sample of DOGs with fainter 24 μm flux densities that have mid-IR bump SEDs (R. S. Bussmann et al. 2009, in preparation). In Section 2, we detail the sample selection, observations, and data reduction. Section 3 contains a description of the methods we use in our morphological analysis, and in Section 4, we report the results of this analysis. In Section 5, we estimate some intrinsic properties of the DOGs in our sample, and we compare our findings with what is seen in other high-redshift galaxy populations. Finally, we present our conclusions in Section 6.

Throughout this paper, we assume H_0 =70 km s^{-1} Mpc^{-1}, $\Omega_{\rm m} = 0.3$, and $\Omega_\lambda = 0.7$. At $z = 2$, this results in 8.37 kpc/″.

2. DATA

In this section, we describe our sample selection and give details regarding the *HST* observations and our data-reduction procedure, as well as how we measure our photometry. Finally, we show postage stamp images and provide a brief qualitative description of each target.

2.1. Sample Selection

As outlined in Section 1, a sample of ≈2600 DOGs from Dey et al. (2008) was originally identified using the 9.3 deg^2 Boötes field of the NDWFS. For details of the selection criteria and photometric analysis, we refer the reader to Dey et al. (2008). In this paper, we analyze *HST* imaging from program HST-GO10890 of 31 of the brightest DOGs at 24 μm (all have $F_{24\,\mu{\rm m}} > 0.8$ mJy). The bolometric luminosity of DOGs with bright 24 μm flux densities is typically dominated by AGN emission, while the opposite is true for 24 μm faint DOGs (0.1 mJy $< F_{24\,\mu{\rm m}} <$ 0.3 mJy), which are dominated by star formation (Pope et al. 2008). Additionally, IRAC photometry shows that the objects in this paper are dominated by a power-law component in the mid-IR. The most likely cause of this emission is the presence of warm dust heated by an AGN (Donley et al. 2007).

Shallow X-ray coverage of the Boötes field exists and has yielded a full catalog of X-ray sources (Murray et al. 2005; Kenter et al. 2005; Brand et al. 2006). Within a 2″ search radius, two of the DOGs studied in this paper (SST24 J143102.2+325152 and SST24 J143644.2+350627) have a single X-ray counterpart, and one DOG has two counterparts (SST24 J142644.3+333051). A full analysis of the X-ray data is beyond the scope of this paper, but these basic results suggest that most DOGs are either not strong X-ray emitters or are heavily obscured. The latter view is supported both by mid-IR spectral features and the fact that this subset of 24 μm bright DOGs shows some of the reddest $R -$ [24] colors of the entire DOG population. Figure 1 shows the color–magnitude diagram in $R -$ [24] versus [24] space for the full DOG population in Boötes and highlights the subsample of objects studied in this paper.

Previous work has shown that objects dominated by a power-law signature in the mid-IR tend to have AGN indicators in their mid-IR spectra, usually silicate absorption but no polycyclic aromatic hydrocarbon (PAH) emission (Weedman et al. 2006a; Polletta et al. 2008; Brand et al. 2008). Indeed, IRS spectra of these sources have revealed redshifts based on the 9.7 μm silicate absorption feature, and all are located at $z \sim 2$. Of the 31 objects in this sample, 17 have spectra from Houck et al. (2005), two have spectra from Weedman et al. (2006b), and the remaining spectra will be presented in a future work (Higdon et al. 2009, in preparation). Subsequent Keck/NIRSPEC (Brand et al. 2007), Keck/LRIS, and Keck/DEIMOS spectroscopy has yielded more precise redshifts for four of the DOGs. The redshift distribution of the sample studied in this paper compared to the overall distribution of spectroscopic redshifts for the DOGs from the Boötes field is shown in Figure 2.

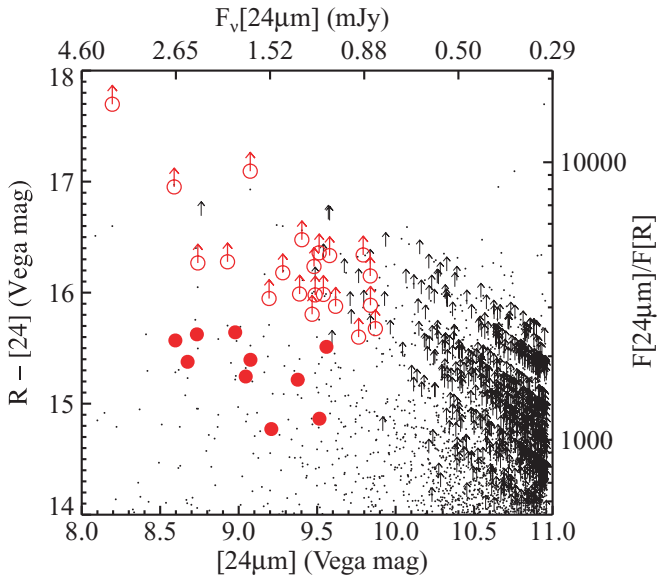

Figure 1. $R - [24]$ color vs. 24 μm magnitude distribution for DOGs in the NDWFS Boötes field. Bottom and top abscissae show the 24 μm magnitude and flux density, respectively, and the left and right ordinates show the color in magnitudes and the $F_{24\,\mu m}/F_R$ flux density ratio, respectively. Black dots and upward arrows show the full sample of DOGs, with and without an *R*-band detection, respectively. The subsample studied in this paper is represented by red circles (open symbols show lower limits).

(A color version of this figure is available in the online journal.)

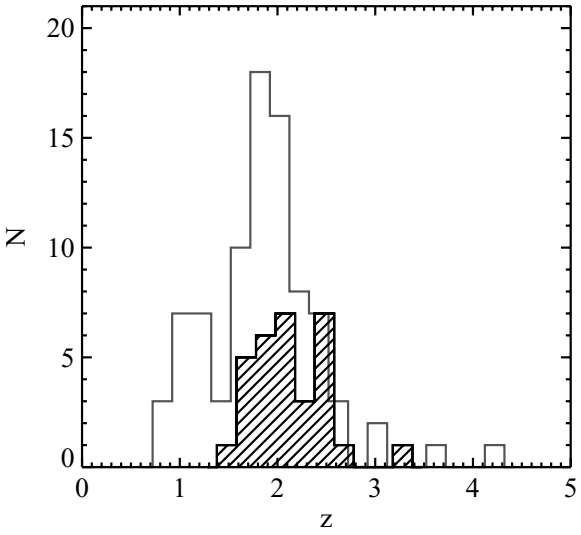

Figure 2. Distribution of redshifts for DOGs in the Boötes Field with spectroscopic redshifts (either from *Spitzer*/IRS or Keck DEIMOS/LRIS). The redshift distribution of the subsample of objects studied in this paper is shown with the hatched histograms and is representative of the full sample of DOGs.

2.2. Observations

Thirty one DOGs we study here were observed with *HST* from 2006 November to 2008 February. Nine were imaged in the Wide Field Channel (WFC) mode of ACS (Ford et al. 1998) before the failure of the instrument. We have observed the remaining 22 DOGs with WFPC2 (Trauger et al. 1994). All 31 DOGs were observed with the NICMOS NIC2 camera. Table 1 summarizes the details of the observations. All data were processed using IRAF.[13] In the following sections, we provide more details about the processing of the ACS, WFPC2, and NICMOS images used in this paper.

2.2.1. ACS

Each DOG was observed over a single orbit through the F814W filter using a four-point dither pattern (ACS–WFC–DITHER–BOX) with a point spacing of 0.″265, a line spacing of 0.″187 and a pattern orientation of 20.°67. Total exposure time was ≈2000 s. Bias subtraction and flat fielding were performed using the standard ACS pipeline (Pavlovsky et al. 2005). The MultiDrizzle routine was used to correct for geometric distortions, perform sky subtraction, image registration, cosmic-ray rejection and final-drizzle combination (Koekemoer et al. 2002). We used a square interpolation kernel and set the output pixel scale at 0.″05 pix^{-1}.

2.2.2. WFPC2

Following the failure of ACS in the middle of Cycle 15 observing, the Wide Field Camera CCD 3 of WFPC2 was used to image the remainder of the DOG population. For these observations, single-orbit data through the F606W filter were used to take advantage of WFPC2's superior sensitivity at this wavelength compared to other WFPC2 filters. We used a four-point dither pattern (WFPC2-BOX) with a point and line spacing of 0.″559 and a pattern orientation of 26.°6. Total exposure time was ≈1600 s. The standard WFPC2 pipeline system was used to bias subtract, dark subtract, and flat field the images (Mobasher et al. 2002). MultiDrizzle was then used to correct for geometric distortions, perform sky subtraction, image registration, cosmic-ray rejection, and final-drizzle combination (Koekemoer et al. 2002). We used a square interpolation kernel and output pixel scale of 0.″045 pix^{-1}, leading to a per pixel exposure time of ≈340 s. Due to the irregular performance of WF4 and the PC CCDs, we have restricted our analysis to the WF2 and WF3 CCDs.

2.2.3. NICMOS

Single-orbit data of the DOGs were acquired with NIC2 and the F160W filter. We used a two-point dither pattern (NIC–SPIRAL–DITH) with a point spacing of 0.″637. Total exposure time was ≈2600 s. To reduce the data, we followed the standard reduction process outlined in the NICMOS data handbook (McLaughlin & Wiklind 2007). We used the IRAF routine `nicpipe` to preprocess the data, followed by the `biaseq` task to correct for nonlinear-bias drifts and spatial-bias jumps. We then used `nicpipe` a second time to do flat fielding and initial cosmic-ray removal. The IRAF task `pedsky` was used to fit for the sky level and the quadrant-dependent residual bias. Significant residual background variation remained after this standard reduction process. To minimize these residuals, we constructed a normalized, object-masked median sky image based on all of our NIC2 science frames. This sky image was then scaled by a constant factor and subtracted from each science image. The scaling factor was computed by minimizing the residual of the difference between the masked science image and the scaled sky image. Mosaicking of the dithered exposures was performed using `calnicb` in IRAF, resulting in a pixel scale of 0.″075 pix^{-1}.

[13] IRAF is distributed by the National Optical Astronomy Observatories, which are operated by the Association of Universities for Research in Astronomy, Inc., under cooperative agreement with the National Science Foundation. http://iraf.noao.edu/

Table 1
Observations

Source Name	R.A. (J2000)	Decl. (J2000)	z	Optical Exposures		Infrared Exposures		ID[g]
				Instrument/Filter	UT Date	Instrument/Filter	UT Date	
SST24 J142538.2+351855	14:25:38.155	+35:18:56.19	2.26[a]	WFPC2/F606W	2007-04-29	NIC2/F160W	2007-06-16	19
SST24 J142622.0+345249	14:26:22.032	+34:52:49.69	2.00[c]	ACS/F814W	2006-11-25	NIC2/F160W	2007-03-13	9
SST24 J142626.4+344731	14:26:26.538	+34:47:31.53	2.13[a]	WFPC2/F606W	2007-12-31	NIC2/F160W	2007-01-04	16
SST24 J142644.3+333051	14:26:44.321	+33:30:52.20	3.312[d]	WFPC2/F606W	2007-04-10	NIC2/F160W	2007-02-25	31
SST24 J142645.7+351901	14:26:45.701	+35:19:01.17	1.75[a]	WFPC2/F606W	2007-04-24	NIC2/F160W	2007-05-05	2
SST24 J142648.9+332927	14:26:48.970	+33:29:27.56	2.00[c]	ACS/F814W	2007-01-17	NIC2/F160W	2006-12-19	10
SST24 J142653.2+330220	14:26:53.285	+33:02:21.37	1.86[a]	ACS/F814W	2006-12-29	NIC2/F160W	2007-03-01	6
SST24 J142804.1+332135	14:28:04.133	+33:21:34.97	2.34[a]	WFPC2/F606W	2007-04-17	NIC2/F160W	2007-05-01	20
SST24 J142924.8+353320	14:29:24.811	+35:33:21.30	2.73[a]	WFPC2/F606W	2007-03-18	NIC2/F160W	2007-02-13	30
SST24 J142958.3+322615	14:29:58.354	+32:26:15.17	2.64[a]	WFPC2/F606W	2007-03-14	NIC2/F160W	2007-06-22	29
SST24 J143001.9+334538	14:30:01.910	+33:45:38.54	2.46[a]	WFPC2/F606W	2007-04-12	NIC2/F160W	2007-04-28	22
SST24 J143025.7+342957	14:30:25.764	+34:29:57.29	2.545[e]	WFPC2/F606W	2007-04-26	NIC2/F160W	2007-04-13	26
SST24 J143102.2+325152	14:31:02.220	+32:51:52.10	2.00[b]	WFPC2/F606W	2007-04-26	NIC2/F160W	2008-01-07	11
SST24 J143109.7+342802	14:31:09.823	+34:28:02.34	2.10[c]	WFPC2/F606W	2007-04-12	NIC2/F160W	2007-01-04	13
SST24 J143135.2+325456	14:31:35.309	+32:54:56.84	1.48[c]	WFPC2/F606W	2007-03-21	NIC2/F160W	2007-06-17	1
SST24 J143225.3+334716	14:32:25.433	+33:47:16.67	2.00[c]	ACS/F814W	2006-12-07	NIC2/F160W	2007-06-17	12
SST24 J143242.5+342232	14:32:42.569	+34:22:32.23	2.16[a]	WFPC2/F606W	2007-04-19	NIC2/F160W	2007-12-07	18
SST24 J143251.8+333536	14:32:51.873	+33:35:35.89	1.78[a]	WFPC2/F606W	2007-03-20	NIC2/F160W	2008-01-14	3
SST24 J143312.7+342011	14:33:12.734	+34:20:11.10	2.119[d]	WFPC2/F606W	2007-04-20	NIC2/F160W	2007-06-19	15
SST24 J143325.8+333736	14:33:25.884	+33:37:36.90	1.90[c]	WFPC2/F606W	2007-05-01	NIC2/F160W	2007-04-20	7
SST24 J143358.0+332607	14:33:58.077	+33:26:07.46	2.414[f]	ACS/F814W	2006-12-10	NIC2/F160W	2008-01-24	21
SST24 J143447.7+330230	14:34:47.762	+33:02:30.46	1.78[a]	WFPC2/F606W	2007-03-19	NIC2/F160W	2006-12-23	4
SST24 J143504.1+354743	14:35:04.166	+35:47:43.79	2.13[a]	WFPC2/F606W	2007-04-26	NIC2/F160W	2007-01-03	17
SST24 J143508.4+334739	14:35:08.518	+33:47:39.44	2.10[c]	WFPC2/F606W	2007-04-12	NIC2/F160W	2007-04-22	14
SST24 J143520.7+340418	14:35:20.801	+34:04:18.30	1.79[a]	WFPC2/F606W	2007-03-16	NIC2/F160W	2007-01-03	5
SST24 J143523.9+330706	14:35:24.005	+33:07:06.84	2.59[a]	ACS/F814W	2007-01-01	NIC2/F160W	2007-01-06	27
SST24 J143539.3+334159	14:35:39.360	+33:41:59.20	2.62[a]	WFPC2/F606W	2008-05-13	NIC2/F160W	2007-02-15	28
SST24 J143545.1+342831	14:35:45.137	+34:28:31.42	2.50[c]	ACS/F814W	2006-12-06	NIC2/F160W	2007-02-15	23
SST24 J143644.2+350627	14:36:44.269	+35:06:27.12	1.95[a]	WFPC2/F606W	2008-01-07	NIC2/F160W	2007-03-14	8
SST24 J143725.1+341502	14:37:25.186	+34:15:02.37	2.50[c]	ACS/F814W	2007-01-07	NIC2/F160W	2007-01-18	24
SST24 J143808.3+341016	14:38:08.352	+34:10:15.55	2.50[c]	ACS/F814W	2006-12-28	NIC2/F160W	2007-02-16	25

Notes.
[a] Redshift from *Spitzer*/IRS (Houck et al. 2005)
[b] Redshift from *Spitzer*/IRS (Weedman et al. 2006a)
[c] Redshift from *Spitzer*/IRS (Higdon et al. 2009, in preparation)
[d] Redshift from Keck NIRSPEC (Brand et al. 2007)
[e] Redshift from Keck DEIMOS
[f] Redshift from Keck LRIS
[g] Panel number in Figure 3

2.3. Astrometry

Each ACS/WFPC2 and NICMOS image is aligned to the reference frame of the NDWFS, which itself is tied to the USNO A-2 catalog. We first run Source Extractor (SExtractor, Bertin & Arnouts 1996) on a cutout of the *I*-band NDWFS corresponding to the appropriate ACS/WFPC2 field of view (FOV) to generate a list of comparison objects. The IRAF task `wcsctran` is used to convert this list into pixel coordinates on the ACS/WFPC2 image. Another IRAF task, `imcentroid`, is used to improve the accuracy of the pixel coordinates. Finally, the IRAF task `ccmap` applies a first-order fit to correct the zero point of the astrometry and update the appropriate WCS information in the header of the ACS/WFPC2 image. This aligned ACS/WFPC2 image is then used as the reference frame for correcting the astrometry of the NICMOS image and the IRAC images (since the IRAC images of the Boötes Field are not tied to the USNO A-2 catalog, but instead to the 2 μm All-Sky Survey frames, see Eisenhardt et al. 2004). Using the properly aligned, multi-wavelength data set, identifying the proper counterpart to the MIPS source is relatively straightforward, since inspection of the four IRAC channels reveals a single source associated with the 24 μm emission for all but one source (this source is undetected in all four IRAC channels). The absolute uncertainty in the centroid of the IRAC 3.6 μm emission ranges from 0.″3 to 0.″5.

2.4. Photometry

We perform 2″ diameter aperture photometry on each DOG in both the rest-optical and rest-UV, choosing the center of the aperture to be located at the peak flux pixel in the NICMOS images. We remove foreground and background objects using SExtractor (see Section 4.2.2) and calculate the sky level using an annulus with an inner diameter of 2″ and a width of 1″. We found that in some cases (particularly those NICMOS images where significant residual nonlinearities remained), the flux density radial profile did not flatten at large radii. When this occurred, we determined the appropriate sky value by the trial-and-error method. We computed the background level and photometric uncertainty by measuring the sigma-clipped mean and rms of fluxes measured in N 2″ diameter apertures, where $N \approx 10$ and $N \approx 50$ for the NICMOS and ACS/WFPC2 images, respectively.

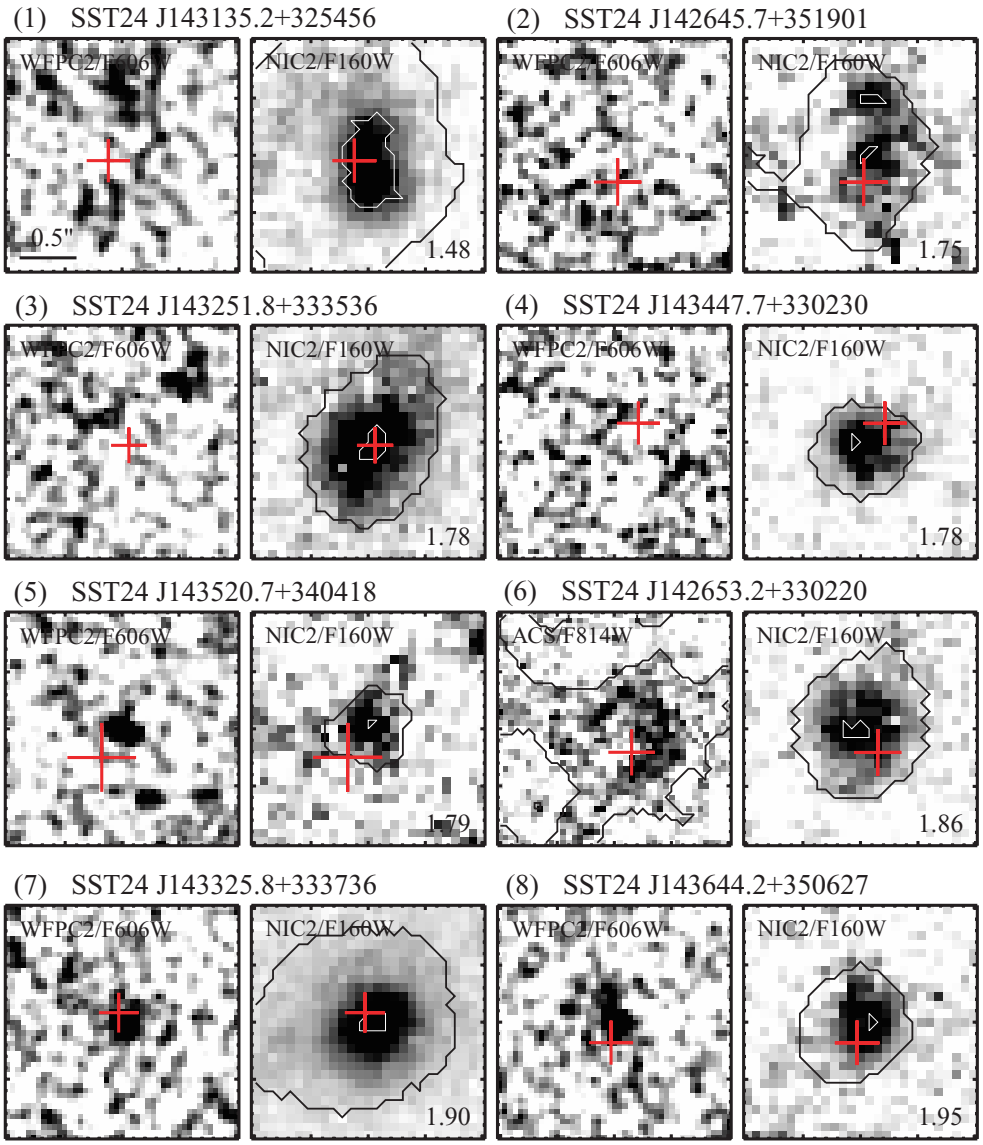

Figure 3. Cutouts of the 31 DOGs observed by *HST*, shown with a linear stretch. Columns 1 and 3 are the rest-UV images from either ACS F814W or WFPC2 F606W. Columns 2 and 4 are the rest-optical images from NIC2 F160W. Each cutout is 2″ on a side and is oriented north up and east left. The objects are arranged in order of increasing redshift, and the redshift is printed in the lower right corner of each NICMOS image. A red cross denotes the position and 1σ uncertainty in the centroid of the IRAC 3.6 μm emission. In NICMOS images, where the S/N per pixel is greater than 2, white contours outline the brightest 20% pixels, and black contours show the outline of the segmentation map used in measuring the nonparametric morphologies.

(A color version of this figure is available in the online journal.)

We compute 4″ diameter aperture photometry in the NDWFS B_W, R, and I images centered on the IRAC 3.6 μm centroid of emission. Sky background levels were computed in a 3″ wide annulus with an inner diameter of 4″. Limiting magnitudes were determined by measuring the flux within a 4″ aperture at several sourceless locations near the DOG and computing the rms variation of the flux values.

We verified the accuracy of our ACS and WFPC2 photometric zero points by comparing well-detected sources common to both our *HST* and NDWFS imaging. For our ACS/F814W observations, we compared to the NDWFS I-band imaging and found negligible offsets (-0.03 ± 0.10 magnitudes). For our WFPC2/F606W observations, we compared to the NDWFS R-band (after correcting for color terms due to the dissimilarity of the R and F606W filter bandpasses) and again found negligible offsets (0.05 ± 0.15 magnitudes).

2.5. Images of DOGs

Figure 3 shows 2″ × 2″ cutout images of the DOGs in order of increasing redshift. Each cutout is centered roughly on the centroid of emission as seen in the NICMOS image. A red plus sign shows the centroid of IRAC 3.6 μm emission and is sized to represent the 1σ uncertainty in the position, which includes independent contributions from the centroiding error on the 3.6 μm emission (≈0.″2–0.″4, depending on the signal-to-noise ratio (S/N)), the relative astrometric calibration uncertainty within the 3.6 μm map (≈0.″2), and the uncertainty in tying the 3.6 μm map to the *HST* images (≈0.″1). The 1σ rms offset between IRAC and NICMOS centroids of the sample is 0.″2. In most cases, the offset in centroids is negligible, but those cases where it is not are associated with faint 3.6 μm emission (when the absolute astrometric uncertainty may be as large as 0.″5).

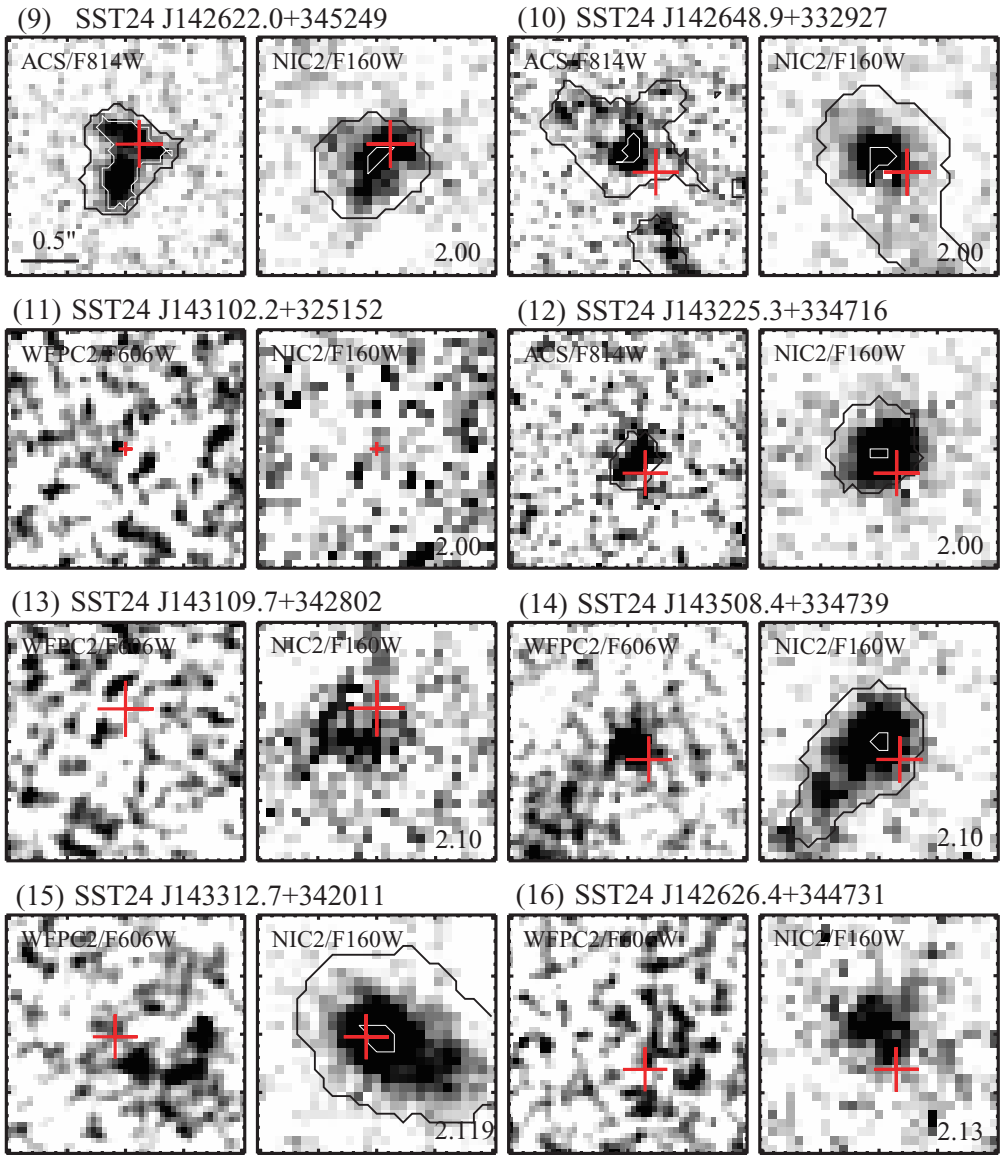

Figure 3. (Continued)

This suggests there is no significant offset between the near-IR and mid-IR centroids, although we note that we cannot rule out offsets at the <1 kpc scale.

The DOGs exhibit a wide range of morphologies, with most being well resolved. Only one object (SST24 J142644.3+333051) shows strong Airy rings and is clearly an unresolved point source. Here we give a brief qualitative description of the morphology of each object.

1. **SST24 J143135.2+325456:** F606W: weak detection. F160W: large-scale emission with a faint tail extending northeast.
2. **SST24 J142645.7+351901:** F606W: no significant detection. F160W: two compact, resolved components separated by $\approx 0\farcs5$.
3. **SST24 J143251.8+333536:** F606W: faint emission slightly northeast (NE) of NICMOS centroid; possible second source $\sim 0\farcs5$ northwest (NW) of NICMOS centroid. F160W: extended object; possible point-source contamination.
4. **SST24 J143447.7+330230:** F606W: no significant detection. F160W: irregular, diffuse object.
5. **SST24 J143520.7+340418:** F606W: compact, resolved object. F160W: very compact object, but no evidence for Airy rings.
6. **SST24 J142653.2+330220:** F814W: large-scale, irregular, and diffuse emission. F160W: large-scale, irregular, and diffuse, but with bright compact nuclear component.
7. **SST24 J143325.8+333736:** F606W: compact, resolved object. F160W: bright compact and extended components.
8. **SST24 J143644.2+350627:** F606W: compact, resolved object. F160W: extended object; possible point-source contamination. This object has a counterpart in the XBoötes catalog (Brand et al. 2006).
9. **SST24 J142622.0+345249:** F814W: four compact, resolved clumps spread in a 'T' shape with no visible central component. F160W: similar irregular 'T' shape, but components are not as distinct. NE component is bluer than other components.

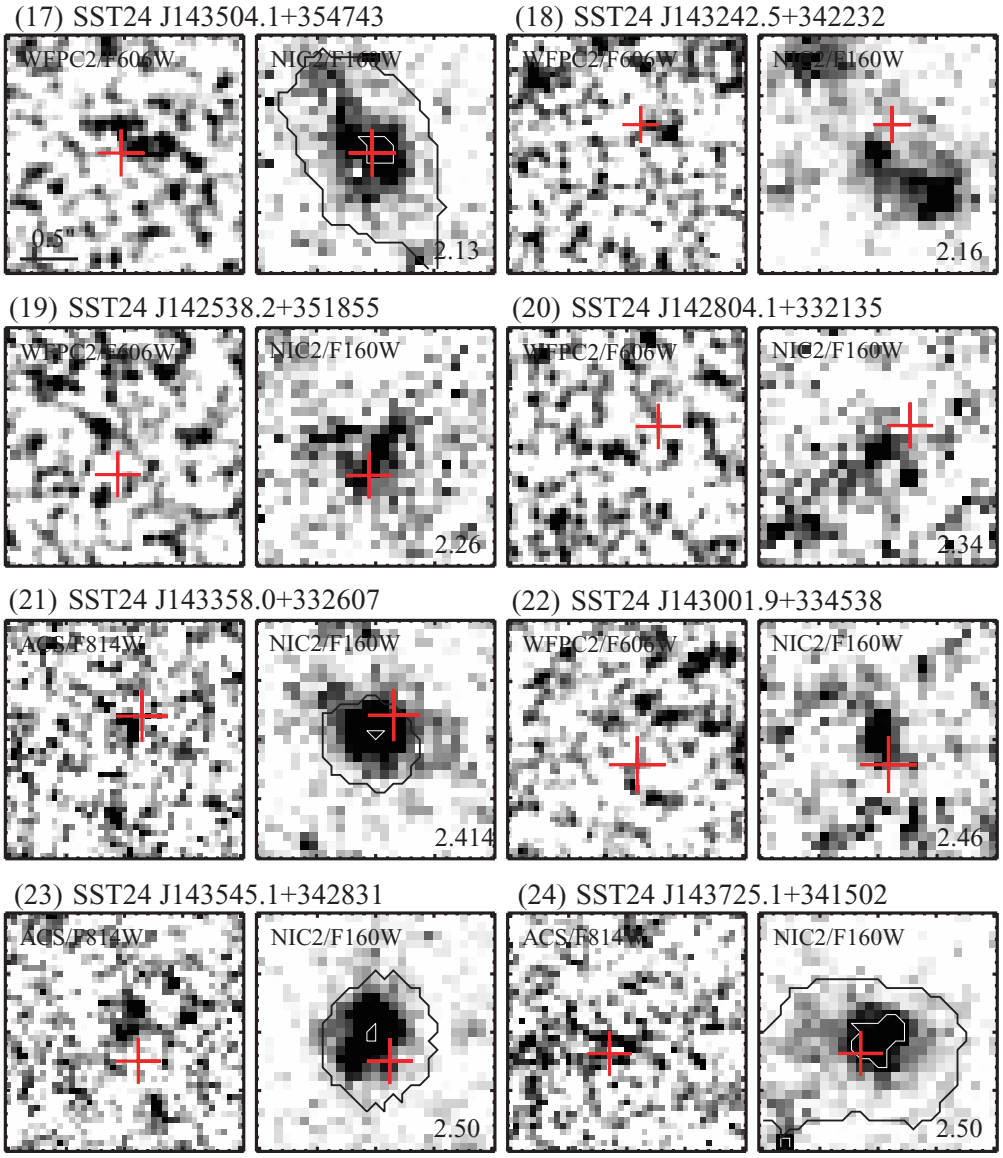

Figure 3. (Continued)

10. **SST24 J142648.9+332927:** F814W: compact, resolved object. Chain of sources extends toward southwest. One of these sources is within 1″ of the DOG and is included in the photometric and morphological measurements, since there is no clear evidence to suggest it is not associated with the system. F160W: similar compact, resolved object; possible point-source contamination.
11. **SST24 J143102.2+325152:** F606W: no significant detection. F160W: no significant detection. This object is also not detected in any of the IRAC images, but does have a counterpart in the XBoötes catalog (Brand et al. 2006).
12. **SST24 J143225.3+334716:** F814W: compact, irregular object. F160W: compact, resolved object; possible point-source contamination.
13. **SST24 J143109.7+342802:** F606W: no significant detection. F160W: irregular, diffuse object.
14. **SST24 J143508.4+334739:** F606W: compact, resolved, and irregular central component with tail of emission to southeast (SE). F160W: very similar, but central component is stronger relative to tail.
15. **SST24 J143312.7+342011:** F606W: four compact components in a semi-circle offset from the centroid of NICMOS emission. F160W: extended object; possible point-source contamination.
16. **SST24 J142626.4+344731:** F606W: no significant detection. F160W: irregular, diffuse object.
17. **SST24 J143504.1+354743:** F606W: faint source barely detected. F160W: irregular, extended object; possible point-source contamination.
18. **SST24 J143242.5+342232:** F606W: no significant detection. F160W: faint, compact component near 3.6 μm centroid with emission leading to second, brighter peak $\sim$0.″5 to southwest (SW). Possible multiple-component system.
19. **SST24 J142538.0+332607:** F606W: no significant detection. F160W: irregular objected elongated in the NW–SE direction.

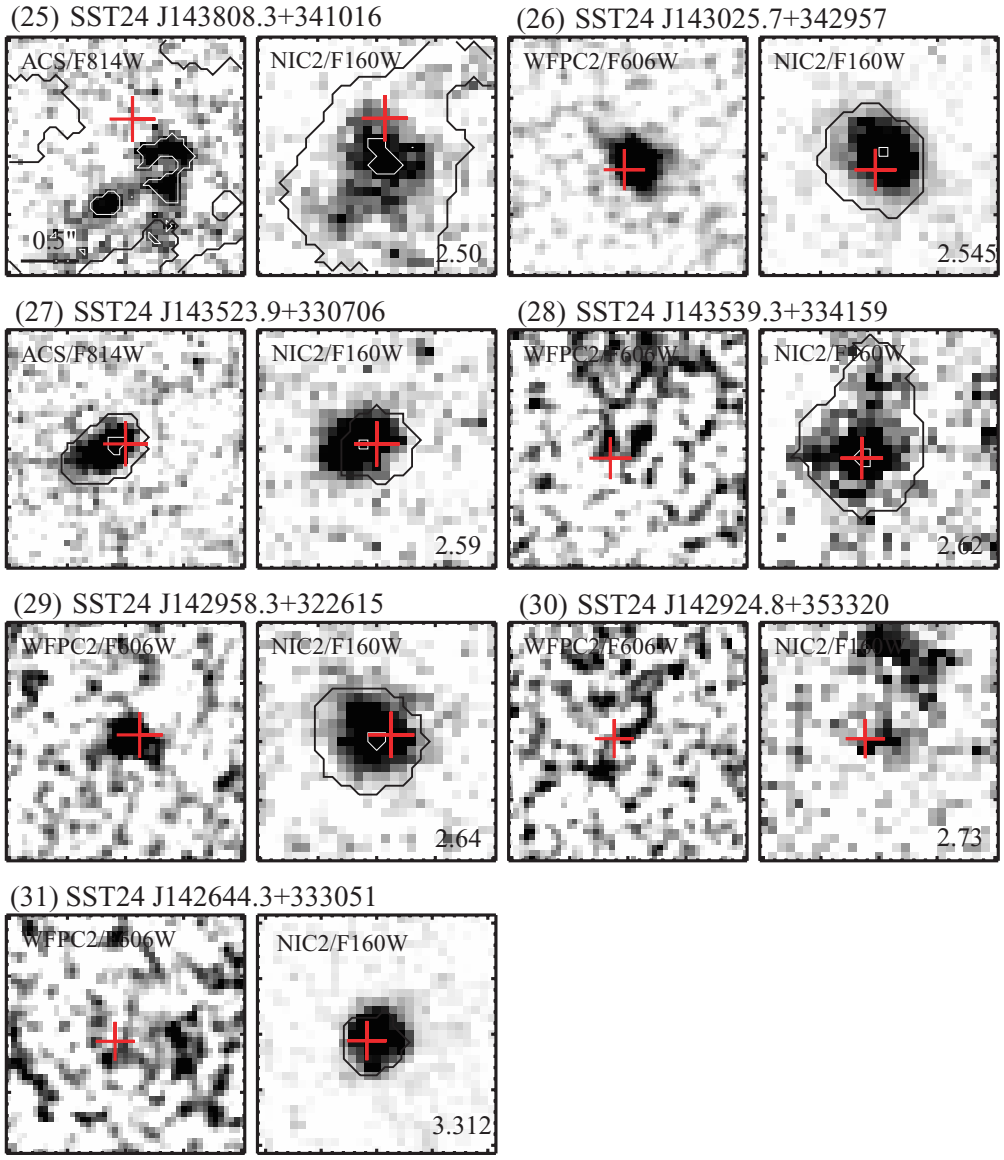

Figure 3. (Continued)

20. **SST24 J142804.1+332135:** F606W: no significant detection. F160W: faint, irregular object.
21. **SST24 J143358.0+332607:** F606W: faint, irregular object. F160W: extended object with possible point-source contamination.
22. **SST24 J143001.9+334538:** F606W: no significant detection. F160W: faint, irregular object.
23. **SST24 J143545.1+342831:** F814W: faint, compact irregular objects; possibly two component system. F160W: extended emission; possible point-source contamination.
24. **SST24 J143725.1+341502:** F814W: very faint, low-surface brightness feature extending to east. F160W: diffuse emission with compact object; faint Airy ring present.
25. **SST24 J143808.3+341016:** F814W: faint, compact, resolved components offset from centroid of NIC2 emission. F160W: compact, central component with extension to SE overlapping ACS emission centroid.
26. **SST24 J143025.7+342957:** F606W: compact, resolved object. F160W: compact, resolved object; possible point-source contamination.
27. **SST24 J143523.9+330706:** F814W: compact, resolved object with tail of emission to SE; possible point-source contamination. F160W: compact, resolved object; possible point-source contamination.
28. **SST24 J143539.3+334159:** F606W: possible faint diffuse emission north of NIC2 centroid. F160W: compact, resolved object; possible point-source contamination; possible tail of emission toward N.
29. **SST24 J142958.3+322615:** F606W: compact resolved object; possible point-source contamination. F160W: extended object with a bright nuclear source; possible point-source contamination.
30. **SST24 J142924.8+353320:** F606W: no significant detection. F160W: very compact, irregular, faint object near IRAC 3.6 μm centroid. Larger, brighter object $\sim$0.″8 to north.
31. **SST24 J142644.3+333051:** F606W: weak detection. F160W: dominated by point-source emission; clear Airy ring. This source has two X-ray counterparts in the XBoötes catalog (Brand et al. 2006).

3. METHODOLOGY: MORPHOLOGICAL ANALYSIS

We undertook three different complementary approaches to analyzing the morphology of the DOGs in our sample: a visual classification experiment, multi-component GALFIT modeling, and nonparametric quantification. In this section, we describe the details of our methodology. The results are described in Section 4.

3.1. Visual Classification

We first undertook a visual classification of the DOGs by conducting the following experiment: for each ACS/WFPC2 image, we generate a 5 arcsec × 5 arcsec cutout image of both the DOG and 14 other randomly selected galaxies in the same FOV with the same magnitude range as our DOG sample. Eight of the coauthors then classified all 15 galaxies in each FOV (the DOG was not identified), placing them into one of the following bins: elliptical/compact (E/C), disk, irregular/multi-component, irregular/diffuse, or too faint to tell. In practice, since these galaxies are selected to be faint in the optical and generally have low S/N, we group together the E/C and disk categories into a "Regular" bin and the two irregular categories into an "Irregular" bin. This results in a total of 3600 independent classifications, of which 240 pertain to the DOGs. In an effort to explore the robustness of our results, we flag and remove from the sample all objects where fewer than six classifiers were in agreement. This has the effect of reducing the fraction of "Too Faint To Tell" responses, but the ratio of the regular to irregular classifications changes by less than 15%. A similar experiment was done on the NICMOS images, without the control sample, since the NIC2 FOV is so small.

Interpretation of the results of our visual classification analysis is hampered by low S/N (in the case of the ACS/WFPC2 images) or the lack of a control sample (in the case of the NICMOS images), so we forego a detailed analysis and instead present the mode of the classifications for each DOG along with an indication of whether the eight coauthors were in general agreement in our morpholical results table in Section 4.2.2. This is useful as a qualitative assessment of the morphology for comparison with the more quantitative methods discussed below.

3.2. GALFIT Modeling

In many of the NICMOS images, there is a compact component that is not seen in the corresponding ACS/WFPC2 image, implying there is significant obscuration in the central region of many of the DOGs. In this section, we describe the method we use to explore the degree to which each DOG is dominated by a central, unresolved component. Our tool in this effort is GALFIT (Peng et al. 2002), which uses a two-dimensional χ^2 minimization to search the parameter space of a set of predefined functions and identify the parameters that best describe the observed two-dimensional profile.

Because the DOGs are small and have low S/N compared to more typical applications of GALFIT, we restrict the size of the fitting region to be 41 × 41 pixels (corresponding to an angular and physical size of 3″ and ≈24 kpc, respectively) and include the minimum necessary components in our model. For a variety of reasons, we expect AGN to be important contributors to the emitted radiation from these sources. Therefore, we model the observed emission with three components which are described by a total of 10 free parameters. The number of degrees of freedom (DOF), $N_{\rm DOF}$, is calculated as the number of pixels in the image being modeled minus the number of free parameters. This implies that the maximum $N_{\rm DOF}$ is 1671. Those cases where $N_{\rm DOF} < 1671$ are associated with images where pixels were masked out because they were associated with residual instrumental noise and prevented convergence with GALFIT. We note that because NIC2 is a Nyquist-sampled array (0.″075 pix^{-1} compared to 0.″16 FWHM beam), the pixels in our image may not be completely independent. As a result, the χ^2_ν values should be interpreted in a relative sense rather than an absolute one.

The first element in our GALFIT model is a sky component whose amplitude is chosen to obtain flat radial profiles at large radii and is not allowed to vary. The second is an instrumental PSF generated from the TinyTim software (Krist & Hook 1997), which can simulate a PSF for NICMOS, WFPC2, and ACS. For the NICMOS and WFPC2 images, the DOG is positioned in nearly the same spot on the camera. In the case of WFPC2, this is pixel (400, 400) of chip 3 and pixel (155, 164) for NICMOS. Meanwhile, a different region of the ACS camera is used for each DOG. Therefore, we generate a unique PSF at each position on the appropriate chip in which a DOG is observed. We use a red power-law spectrum ($F_\nu \propto \nu^{-2}$) as the object spectrum. The PSF is computed out to a size of 3.″0, and for the WFPC2 PSF, we oversample by a factor of 2 to match the pixel scale of the drizzled WFPC2 images.

The final component is a Sérsic profile (Sersic 1968) where the surface brightness scales with radius as $\exp[-\kappa((r/R_{\rm eff})^{1/n}-1)]$, where κ is chosen such that half of the flux falls within $R_{\rm eff}$. We attempted to place as few constraints as possible so as to optimize the measurement of the extended flux (i.e., the nonpoint-source component). However, in certain cases, the Sérsic index had to be constrained to be positive to ensure convergence on a realistic solution. For the NICMOS images, we used the uncertainty image output by `calnicb` as the error image required by GALFIT to perform a proper χ^2 minimization. The TinyTim NIC2 PSF is convolved with the Sérsic profile prior to performing the χ^2 minimization. The initial guesses of the magnitude, half-light radius, position angle, and ellipticity were determined from the output values from SExtractor. Varying the initial guesses within reasonable values (e.g., plus or minus two pixels for the half-light radius) yielded no significant change in the best-fit model parameters. We used the NICMOS centroid as the initial guess for the (x, y) position of both the PSF and extended components, but in a few cases these guesses had to be modified by 1–2 pixels in order to result in convergence.

We note that we tested two-component models as well (single-component Sérsic profile plus sky background) and found larger reduced χ^2 values, especially when the point-source fraction in our three-component model was large (see further discussion in Section 4.2.1). In cases where the point-source fraction was small, the two-component model had similar parameter values as the three-component model, as we would expect.

It is important to note here that NIC2 cannot spatially resolve objects smaller than 1.3 kpc at $z \approx 2$. This limit is large enough to encompass a compact stellar bulge as well as an active galactic nucleus, implying that we cannot, from these data alone, distinguish between these two possibilities as to the nature of the central, unresolved component.

After the best-fit parameters are found in the NICMOS image, we run GALFIT with a simplified model on the DOGs in the ACS/WFPC2 images. The primary simplification is to fix the position of the PSF based on the best-fit NICMOS PSF location (allowing up to two pixel wiggle room to account for astrometric uncertainties, which can be as large as 0.″1). In many cases,

GALFIT required an upper limit to be placed on the magnitude of the PSF component in order to reach convergence. We choose to use the magnitude of a point source detected at the 2σ level for this upper limit. We note that our Sérsic profile model for the extended DOG flux is not representative of the rest-UV morphology of many of the DOGs (i.e., the reduced χ^2 values are large), but it does adequately recover their total flux.

3.3. Nonparametric Classification

The Gini coefficient (G) and M_{20} parameter are known to be reliable tools for the characterization of faint-object morphologies (Lotz et al. 2004). G was originally created to measure how evenly the wealth in a society is distributed (Glasser 1962). Recently, Abraham et al. (2003) and Lotz et al. (2004) applied this method to aid in the classification of galaxies, with G defined such that low (high) values imply an equal (unequal) distribution of a flux. M_{20} is the logarithm of the second-order moment of the brightest 20% of the galaxy's flux, normalized by the total second-order moment (Lotz et al. 2004). This means that higher values of M_{20} imply multiple bright clumps offset from the second-order moment center. Lower values, on the other hand, suggest a system dominated by a central component.

Prior to computing G or M_{20}, we first generate a catalog of objects using SExtractor. We use a detection threshold of 1.5σ (corresponding to 24.5 mag arcsec^{-2}) and a minimum detection area of 15 pixels. The center of the image as well as the ellipticity and position angle computed by SExtractor are used as inputs for computing morphological measures. In addition, we use catalog sources selected to have magnitudes within the range of all 24 DOGs analyzed in this paper as a "field" galaxy sample for comparison to DOGs.

Much of the methodology in this section relies on the morphology code written by J. Lotz and described in detail in Lotz et al. (2004). Here, we summarize the relevant information. Postage stamps of each object in the SExtractor catalog (and the associated segmentation map) are created with foreground/background objects masked out. Using a small region of the cutout devoid of sources, a sky value is computed and subtracted from the postage stamp. Next, we determine which pixels in each postage stamp belong to the galaxy and which do not. Since the isophotal-based segmentation map produced by SExtractor is subject to the effects of surface brightness dimming at high redshift, we use a segmentation map based on the mean surface brightness at the Petrosian radius $\mu(R_p)$. Pixels with surface brightness above $\mu(R_p)$ are assigned to the galaxy, while those below it are not. We define $R_{\rm p}$ as the radius at which the ratio of the surface brightness at $R_{\rm p}$ to the mean surface brightness within $R_{\rm p}$ is equal to 0.2.

Using the new segmentation map, we recompute the galaxy's center by minimizing the total second-order moment of the flux. A new value of $R_{\rm p}$ is then computed and a revised segmentation map is used to calculate G and M_{20}. Finally, the morphology code produces an average S/N per pixel value using the pixels in the revised segmentation map (Equations (1)–(5) in Lotz et al. 2004).

One of the most common methods of characterizing galaxy morphologies in the literature is to measure the concentration index C (Abraham et al. 1994), the rotational asymmetry A (Schade et al. 1995), and the residual clumpiness, S (Conselice 2003). Given sufficiently high S/N and spatial resolution, the *CAS* system has had demonstrated success in measuring morphological parameters and identifying mergers at low (Conselice 2003) and high redshift (Conselice et al. 2008). Unfortunately, the objects in our sample do not meet simultaneously the S/N and spatial-resolution requirements to be reliably placed in *CAS* space. Because computation of A and S involves differencing two images, the necessary per pixel S/N to measure these parameters reliably is twice as high as those that do not involve subtracting images. We find per pixel S/N values ranging from $\sim$ 2–5 for the DOGs, whereas reliable measurements of A and S require S/N$\geqslant$5 (Lotz et al. 2004). In principle, the data are of sufficient quality to measure C (see Table 5), but in practice we find that the inherent assumption of circular symmetry does not apply well to the DOGs, making the interpretation of C values difficult.

4. RESULTS

4.1. Photometry

In Figure 4, we show the color–magnitude diagram for DOGs and a sample of galaxies in the HDF whose photometric redshifts are comparable to DOGs ($1.5 < z_{\rm phot} < 2.5$). For DOGs, where the measured flux is below the 2σ detection limit, we use an open-plotting symbol and an upward-pointing arrow. DOGs range in H-band magnitude from 21.93 to 25.1 AB mags. In both $V - H$ and $I - H$, DOGs are redder than a typical high-z galaxy by 0.2–3 AB mags. In particular, the LBGs from the HDF-N (Papovich et al. 2001) are comparably bright in H, but fainter in V by $\approx$2 AB mags than DOGs. There is a substantial overlap between the colors of DOGs and DRGs, suggesting that we might expect to see similarities in the morphologies between these two populations. Table 2 summarizes the photometric information derived from the NDWFS and the *HST* imaging.

4.2. Morphologies

4.2.1. GALFIT Results

The results of our GALFIT analysis for the extended component Sérsic profile fit to the NICMOS images are shown in Table 3, along with 1σ uncertainties in the best-fit parameters. The Sérsic indices (n) range from 0.1 to 2.2 (median $n = 0.9$). For those objects where $n < 1$, we note that constraining n to be equal to 1 does not significantly alter the remaining fit parameters. As the Sérsic index decreases, the radial profile flattens more rapidly within $r < R_{\rm eff}$, and the intensity drops more steeply beyond $r > R_{\rm eff}$. For reference, $n = 0.5$ corresponds to a Gaussian profile, $n = 1$ corresponds to an exponential profile, and $n = 4$ corresponds to a de Vaucouleurs profile (Peng et al. 2002). The ratio of the minor-to-major axis ranges from 0.20 to 0.88 with a median value of 0.53. In comparison, simulated merger remnants tend to have a luminous component in the shape of an oblate spheroid, with axis ratios of 1:1:0.5 (Novak et al. 2006). The projected axial ratio should thus vary between 0.5 and 1.0. Our observed median value of $\approx$0.5 suggests that DOGs have more disk-like profiles than the simulated merger remnants. This may be due to a nonmerger origin for DOGs, or it may be an indication that DOGs have not progressed to the merger remnant stage.

It is possible for a degeneracy to arise in the fitting parameters, in the sense that a high-n, low-point-source fraction model may be comparable to a low-n, high-point-source fraction model. We have tested this by running GALFIT with the point-source fraction set to zero (i.e., removing the PSF component). The resulting n values range from 0.1 to 5.2 with a median of 2.0, which is still below the value of 4 that is typical of

Table 2
Photometric Properties[a,b]

Source Name	B_W	R	I	V (F606W)	I (F814W)	H (F160W)	F_{24} (mJy)	$R-[24]$[c]
SST24 J142538.2+351855	>26.6	>25.9	>25.5	>26.0	...	24.0 ± 0.1	0.85 ± 0.05	>16.1
SST24 J142622.0+345249	24.5 ± 0.1	24.5 ± 0.3	24.0 ± 0.3	...	24.18 ± 0.06	23.6 ± 0.1	1.29 ± 0.05	15.2
SST24 J142626.4+344731	>26.6	>25.4	>25.2	>26.4	...	23.7 ± 0.1	1.17 ± 0.04	>16.0
SST24 J142644.3+333051	>26.5	24.3 ± 0.2	24.3 ± 0.2	25.9 ± 0.3	...	21.93 ± 0.02	1.14 ± 0.04	14.9
SST24 J142645.7+351901	>26.6	>25.8	24.5 ± 0.3	>26.2	...	23.31 ± 0.09	1.14 ± 0.05	>16.3
SST24 J142648.9+332927	25.1 ± 0.2	>25.0	24.1 ± 0.1	...	24.9 ± 0.2	23.3 ± 0.1	2.33 ± 0.07	>16.3
SST24 J142653.2+330220	>26.6	>26.1	24.7 ± 0.3	...	25.0 ± 0.2	22.7 ± 0.1	0.88 ± 0.05	>16.3
SST24 J142804.1+332135	>26.4	>25.7	>25.3	>26.6	...	25.1 ± 0.5	0.84 ± 0.03	>15.9
SST24 J142924.8+353320	>26.6	>25.4	>24.9	>26.1	...	24.7 ± 0.3	1.04 ± 0.05	>15.9
SST24 J142958.3+322615	25.6 ± 0.1	>25.7	>25.4	25.5 ± 0.3	...	23.26 ± 0.09	1.18 ± 0.05	>16.2
SST24 J143001.9+334538	>26.4	>25.8	>25.1	>26.5	...	24.9 ± 0.3	3.84 ± 0.06	>17.7
SST24 J143025.7+342957	24.6 ± 0.1	24.0 ± 0.1	23.9 ± 0.1	24.21 ± 0.07	...	22.29 ± 0.03	2.47 ± 0.05	15.4
SST24 J143102.2+325152	>25.7	>25.2	>25.2	>26.0	...	>25.1	1.19 ± 0.05	>15.8
SST24 J143109.7+342802	>26.4	>25.5	>25.2	>26.3	...	23.6 ± 0.1	1.11 ± 0.04	>16.0
SST24 J143135.2+325456	24.7 ± 0.1	23.9 ± 0.1	23.5 ± 0.1	25.1 ± 0.2	...	22.04 ± 0.03	1.51 ± 0.05	14.8
SST24 J143225.3+334716	>26.9	>25.3	>25.2	...	26.0 ± 0.4	22.8 ± 0.1	1.28 ± 0.05	>16.0
SST24 J143242.5+342232	>26.5	>25.3	>25.1	>26.7	...	22.68 ± 0.04	0.91 ± 0.04	>15.6
SST24 J143251.8+333536	>26.5	>25.5	>25.1	>26.5	...	22.20 ± 0.03	0.82 ± 0.04	>15.7
SST24 J143312.7+342011	24.5 ± 0.1	24.2 ± 0.2	23.9 ± 0.1	24.7 ± 0.1	...	22.23 ± 0.04	1.76 ± 0.04	15.2
SST24 J143325.8+333736	25.6 ± 0.3	24.6 ± 0.3	23.9 ± 0.2	25.6 ± 0.3	...	21.52 ± 0.03	1.87 ± 0.06	15.6
SST24 J143358.0+332607	>26.7	>25.9	>25.3	...	>25.9	23.09 ± 0.06	1.07 ± 0.04	>16.3
SST24 J143447.7+330230	>26.6	>26.1	>25.2	>26.0	...	23.1 ± 0.1	1.71 ± 0.04	>17.1
SST24 J143504.1+354743	>26.6	>25.8	>25.5	>26.4	...	23.08 ± 0.09	1.26 ± 0.05	>16.5
SST24 J143508.4+334739	24.6 ± 0.1	24.1 ± 0.1	23.8 ± 0.1	23.87 ± 0.05	...	22.69 ± 0.07	2.65 ± 0.08	15.6
SST24 J143520.7+340418	24.8 ± 0.1	> 25.1	24.1 ± 0.2	>26.2	...	24.0 ± 0.2	1.53 ± 0.06	>15.9
SST24 J143523.9+330706	>26.8	25.0 ± 0.2	24.9 ± 0.3	...	24.7 ± 0.2	22.93 ± 0.06	1.09 ± 0.05	15.5
SST24 J143539.3+334159	>26.4	>25.5	24.7 ± 0.3	25.1 ± 0.2	...	23.1 ± 0.1	2.67 ± 0.06	>16.9
SST24 J143545.1+342831	>26.9	>25.2	>25.0	...	>26.7	22.59 ± 0.05	1.95 ± 0.05	>16.3
SST24 J143644.2+350627	24.7 ± 0.1	24.3 ± 0.1	24.0 ± 0.2	25.6 ± 0.2	...	22.70 ± 0.07	2.34 ± 0.05	15.6
SST24 J143725.1+341502	25.4 ± 0.2	>25.4	>25.2	...	26.1 ± 0.6	22.70 ± 0.08	1.41 ± 0.05	>16.2
SST24 J143808.3+341016	25.1 ± 0.1	24.4 ± 0.3	23.9 ± 0.1	...	24.7 ± 0.2	22.34 ± 0.08	1.71 ± 0.05	15.4

Notes.
[a] magnitude lower limits represent 2σ values.
[b] magnitudes given in AB system.
[c] $R-[24]$ color in Vega system.

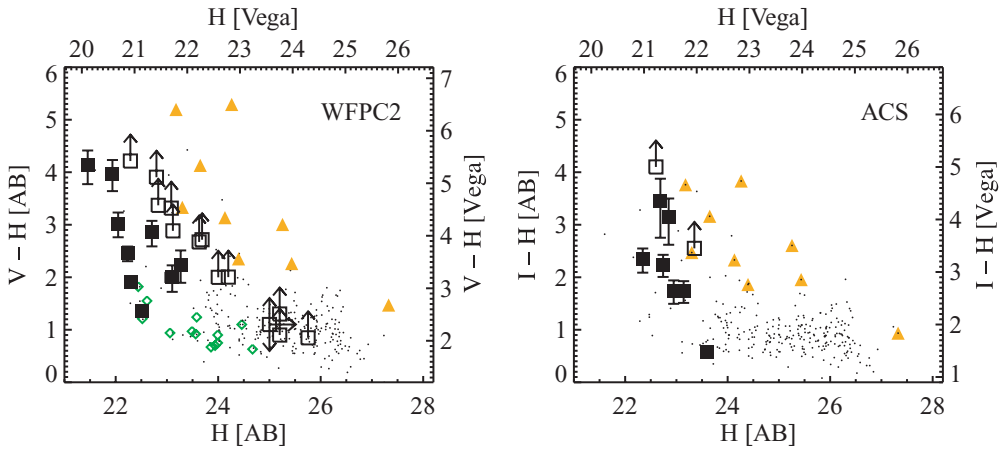

Figure 4. Color–magnitude diagram for DOGs. Left: $V-H$ vs. H for DOGs observed by WFPC2 (filled black squares show detections, open black squares show lower limits). Galaxies spanning the redshift range $1.5 < z < 2.5$ in the HDF-N (C. Papovich, private communication) and HDF-S (Labbé et al. 2003) are shown with black dots. Bright LBGs from the HDF-N are shown with green diamonds (Papovich et al. 2001). DRGs in the HDF-S are represented by filled orange triangles. Right: $I-H$ vs. H for DOGs observed by ACS. Symbols are the same as in left panel.

(A color version of this figure is available in the online journal.)

early-type galaxies. A total of seven DOGs have $n > 3$ using this zero-point-source model. The best-fit $R_{\rm eff}$ values change by less than one pixel, with an offset of -0.2 ± 0.8 pixels. In general, as mentioned in Section 3.2, the removal of the PSF component leads to larger reduced-χ^2 values (see Columns 5 and 6 in Table 3). However, we note that only one case (SST24 J142644.3+333051) is associated with a >0.08 decrease in χ^2_ν after adding a nonzero PSF component. This suggests that the

Table 3
GALFIT Results

Source Name	n	Axial Ratio	$R_{\rm eff}$ (kpc)	χ^2_ν [a]	χ^2_ν [b]	$N_{\rm dof}$
SST24 J142538.2+351855	0.7 ± 0.2	0.64 ± 0.09	2.5 ± 0.4	0.35	0.36	1653
SST24 J142622.0+345249	0.1 ± 0.1	0.55 ± 0.04	2.5 ± 1.0	0.92	0.92	1671
SST24 J142626.4+344731	0.8 ± 0.2	0.59 ± 0.07	3.0 ± 0.4	1.35	1.35	1671
SST24 J142644.3+333051	5.6 ± 3.4	0.71 ± 0.07	1.1 ± 0.3	1.16	2.58	1671
SST24 J142645.7+351901	0.1 ± 0.1	0.41 ± 0.03	4.6 ± 0.2	1.08	1.08	1671
SST24 J142648.9+332927	0.7 ± 0.3	0.70 ± 0.05	1.8 ± 0.1	1.08	1.08	1561
SST24 J142653.2+330220	0.4 ± 0.1	0.85 ± 0.03	2.9 ± 0.1	0.95	0.96	1671
SST24 J142804.1+332135	1.0 ± 0.6	0.19 ± 0.06	6.4 ± 2.6	0.95	0.96	1671
SST24 J142924.8+353320	0.8 ± 0.3	0.35 ± 0.06	2.8 ± 0.4	1.04	1.07	1671
SST24 J142958.3+322615	0.4 ± 0.1	0.78 ± 0.03	2.1 ± 0.1	0.36	0.39	1671
SST24 J143001.9+334538	1.0 ± 1.3	0.6 ± 0.1	1.2 ± 0.3	0.49	0.49	1671
SST24 J143025.7+342957	1.0 ± 0.1	0.52 ± 0.02	1.8 ± 0.1	0.90	0.96	1671
SST24 J143102.2+325152	...	...	...	...	...	...
SST24 J143109.7+342802	1.2 ± 0.4	0.36 ± 0.05	7.0 ± 1.7	1.15	1.15	1671
SST24 J143135.2+325456	0.5 ± 0.1	0.53 ± 0.01	3.8 ± 0.1	1.54	1.56	1671
SST24 J143225.3+334716	0.9 ± 0.2	0.55 ± 0.03	1.9 ± 0.1	0.93	0.94	1671
SST24 J143242.5+342232	2.0 ± 0.4	0.50 ± 0.06	4.0 ± 0.8	0.57	0.58	1601
SST24 J143251.8+333536	0.8 ± 0.1	0.50 ± 0.02	3.3 ± 0.1	0.50	0.52	1671
SST24 J143312.7+342011	0.7 ± 0.1	0.51 ± 0.01	4.0 ± 0.1	0.63	0.66	1671
SST24 J143325.8+333736	1.3 ± 0.1	0.70 ± 0.01	3.1 ± 0.1	0.52	0.60	1671
SST24 J143358.0+332607	2.1 ± 0.5	0.84 ± 0.07	1.4 ± 0.1	0.49	0.48	1671
SST24 J143447.7+330230	0.4 ± 0.1	0.88 ± 0.04	1.9 ± 0.1	0.88	0.89	1671
SST24 J143504.1+354743	0.5 ± 0.1	0.43 ± 0.03	4.6 ± 0.3	0.91	0.93	1671
SST24 J143508.4+334739	2.6 ± 0.4	0.40 ± 0.03	2.2 ± 0.2	1.06	1.10	1671
SST24 J143520.7+340418	0.6 ± 0.4	0.5 ± 0.1	3.4 ± 0.7	1.08	1.10	1671
SST24 J143523.9+330706	0.5 ± 0.1	0.46 ± 0.02	1.5 ± 0.1	1.00	1.05	1671
SST24 J143539.3+334159	1.8 ± 0.5	0.82 ± 0.09	3.7 ± 0.7	0.91	0.92	1671
SST24 J143545.1+342831	1.1 ± 0.2	0.49 ± 0.03	2.2 ± 0.1	1.04	1.06	1671
SST24 J143644.2+350627	0.9 ± 0.2	0.70 ± 0.05	1.9 ± 0.1	1.22	1.23	1670
SST24 J143725.1+341502	0.3 ± 0.1	0.50 ± 0.03	3.4 ± 0.2	1.09	1.14	1424
SST24 J143808.3+341016	0.9 ± 0.1	0.81 ± 0.04	3.0 ± 0.2	1.37	1.38	1671

Notes.
[a] Asssuming finite PSF contribution
[b] Asssuming zero PSF contribution

PSF component in most of the DOGs in this sample is not dominant at rest-frame optical wavelengths.

We find the effective radius, $R_{\rm eff}$, ranges from 1.1 to 5.9 kpc with a median value of 2.5 kpc. In the left panel of Figure 5, we show the distribution of $R_{\rm eff}$ values for DOGs (dark-shaded histogram), Distant Blue Galaxies (diagonal blue hatched; DBGs, i.e., galaxies with $z_{\rm phot} > 2$ that satisfy $J - Ks < 2.3$; Toft et al. 2007), and DRGs (opposite diagonal red hatched; Zirm et al. 2007; Toft et al. 2007). Two-sided K-S tests show that DOGs are dissimilar from both populations, with a $< 7\%$ and $< 4\%$ chance of being drawn from the same parent distribution, respectively. Based on the nature of their UV-NIR SED, DRGs may be separated into those that are actively forming stars (active DRGs or sDRGs) and those that are not (quiescent DRGs or qDRGs, see Zirm et al. 2007; Toft et al. 2007). The right panel of Figure 5 shows the DOG $R_{\rm eff}$ distribution in comparison to active DRGs (diagonal blue hatched) and quiescent DRGs (opposite diagonal red hatched). Quiescent DRGs have much smaller effective radii, while active DRGs are much closer to DOGs. Here, the two-sided K-S test gives a 99.9994% and 34% chance of being drawn from different parent distributions, respectively, suggesting that the DOG and active DRG populations may overlap.

In Table 4, we give the V, I, and H magnitudes of the nuclear (PSF) component and the extended (galaxy) component, as well as the fraction of light contributed by a point source (including 1σ uncertainties). When the nuclear component is not detected, we quote the 3σ limit on the point-source fraction. The magnitude of the PSF component is measured using the same aperture photometry method described in Section 2.4, with the exception that the sky background is assumed to be zero. For the extended component, we subtract the PSF component from the science image and compute the photometry in the usual way on the residual image. The fraction of light due to an unresolved component in the rest-optical ranges from 0.04 to 0.78, and the median is 0.12. In the rest-UV, however, this fraction is significantly smaller, with only one object having a detected fraction. This object, SST24 J143523.9+330706, stands out as unique by virtue of having a greater point-source fraction in the rest UV than in the rest optical. This behavior is unique within our sample (but is expected when the AGN is viewed without obscuration) and is also reflected in the nonparametric measures of its morphology (see Section 4.2.2 for more detail).

Figure 6 shows the $V - H$ and $I - H$ colors of the nuclear, extended, and full galaxy components as a function of H, in AB magnitudes. High-z galaxies and DRGs in the HDF-N and HDF-S are also shown. The full galaxy and extended components have similar colors and H magnitudes, consistent with the nuclear component not dominating the flux. This is why even the extended components of DOGs are redder in both

Table 4
PSF Subtraction Analysis

Source Name	V_{nuc}	I_{nuc}	H_{nuc}	V_{gal}	I_{gal}	H_{gal}	f_{PSF}^{opt}	f_{PSF}^{ir}
SST24 J142538.2+351855	>28.3	...	27 ± 2	>26.0	...	24.1 ± 0.3	...	<0.27
SST24 J142622.0+345249	...	>27.9	27 ± 1	...	24.2 ± 0.1	23.6 ± 0.2	<0.01	<0.15
SST24 J142626.4+344731	>27.6	...	26.8 ± 0.3	>26.4	...	23.7 ± 0.2	...	<0.07
SST24 J142644.3+333051	>28.1	...	22.3 ± 0.1	26.1 ± 0.6	...	23.4 ± 0.1	<0.06	0.73 ± 0.07
SST24 J142645.7+351901	>27.7	...	27 ± 1	>26.2	...	22.9 ± 0.1	...	<0.08
SST24 J142648.9+332927	...	>28.1	25.2 ± 0.3	...	24.9 ± 0.4	23.3 ± 0.2	<0.03	0.15 ± 0.06
SST24 J142653.2+330220	...	>28.3	25.8 ± 0.2	...	25.0 ± 0.4	22.8 ± 0.2	<0.01	0.06 ± 0.03
SST24 J142804.1+332135	>27.7	...	26.1 ± 0.5	>26.6	...	>25.2	...	...
SST24 J142924.8+353320	>27.9	...	25.9 ± 0.5	>26.1	...	>25.3	...	...
SST24 J142958.3+322615	>28.2	...	25.0 ± 0.1	25.6 ± 0.6	...	23.5 ± 0.2	<0.01	0.20 ± 0.03
SST24 J143001.9+334538	>27.9	...	26.6 ± 0.9	>26.5	...	>25.5	...	<0.53
SST24 J143025.7+342957	>28.4	...	23.9 ± 0.1	24.2 ± 0.2	...	22.58 ± 0.07	<0.01	0.24 ± 0.03
SST24 J143102.2+325152	>27.8	...	>27.0	>26.0	...	>25.1	...	...
SST24 J143109.7+342802	>27.9	...	27 ± 1	>26.3	...	23.78 ± 0.3	...	<0.18
SST24 J143135.2+325456	>27.8	...	26.1 ± 0.3	25.2 ± 0.5	...	22.1 ± 0.1	<0.06	<0.02
SST24 J143225.3+334716	...	>28.3	24.8 ± 0.1	...	26 ± 1	23.0 ± 0.2	<0.02	0.17 ± 0.04
SST24 J143242.5+342232	>28.5	...	25.4 ± 0.2	>26.7	...	22.9 ± 0.1	...	0.09 ± 0.03
SST24 J143251.8+333536	>28.7	...	24.9 ± 0.1	>26.5	...	22.4 ± 0.1	...	0.09 ± 0.01
SST24 J143312.7+342011	>27.9	...	24.6 ± 0.1	24.7 ± 0.3	...	22.4 ± 0.1	<0.04	0.12 ± 0.02
SST24 J143325.8+333736	>27.6	...	23.6 ± 0.1	25.8 ± 0.7	...	21.6 ± 0.1	...	0.13 ± 0.02
SST24 J143358.0+332607	...	27.5 ± 0.5	25.8 ± 0.3	...	>25.9	23.5 ± 0.2	...	0.10 ± 0.05
SST24 J143447.7+330230	>27.9	...	25.8 ± 0.6	>26.0	...	23.2 ± 0.2	...	<0.12
SST24 J143504.1+354743	>27.7	...	24.9 ± 0.2	>26.4	...	23.3 ± 0.2	...	0.18 ± 0.05
SST24 J143508.4+334739	27 ± 2	...	24.9 ± 0.3	23.9 ± 0.1	...	22.6 ± 0.1	<0.14	0.11 ± 0.04
SST24 J143520.7+340418	>28.1	...	24.9 ± 0.1	>26.2	...	25.0 ± 0.5	...	0.5 ± 0.1
SST24 J143523.9+330706	...	26.2 ± 0.2	24.9 ± 0.2	...	25.0 ± 0.5	23.1 ± 0.1	0.24 ± 0.04	0.17 ± 0.03
SST24 J143539.3+334159	>28.4	...	25.2 ± 0.2	25.2 ± 0.5	...	23.3 ± 0.3	<0.01	0.15 ± 0.06
SST24 J143545.1+342831	...	>28.0	24.2 ± 0.1	...	>26.7	22.9 ± 0.1	...	0.22 ± 0.03
SST24 J143644.2+350627	28 ± 1	...	24.9 ± 0.3	25.7 ± 0.4	...	22.9 ± 0.1	<0.11	0.13 ± 0.04
SST24 J143725.1+341502	...	>28.1	23.6 ± 0.1	...	>26.2	23.3 ± 0.2	...	0.43 ± 0.05
SST24 J143808.3+341016	...	>28.3	25.9 ± 0.4	...	24.7 ± 0.4	22.4 ± 0.2	<0.01	<0.06

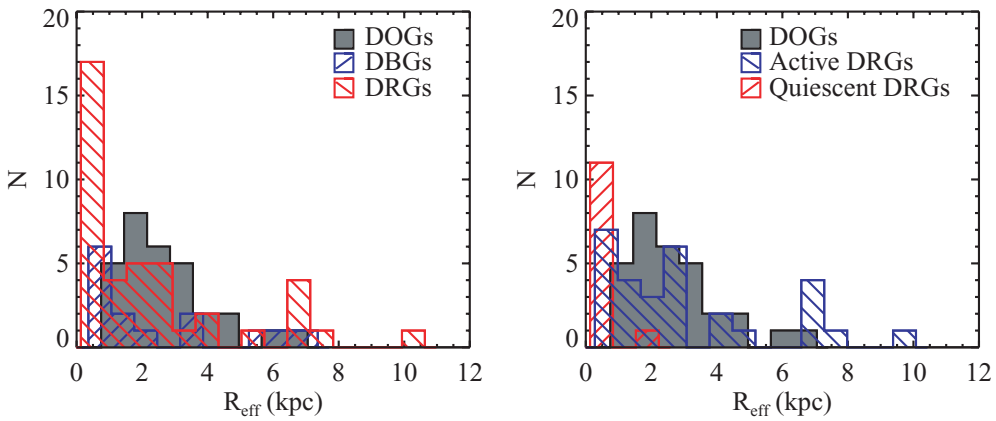

Figure 5. Left: distribution of effective radius, R_{eff}, for an unconstrained Sérsic profile matched to the DOGs using GALFIT (filled grey region), DBGs (Distant Blue Galaxies, diagonal hatched blue region) and DRGs (opposite diagonal hatched red region). Right: distribution of R_{eff} values for DOGs (filled grey region), active DRGs (diagonal hatched blue region), and quiescent DRGs (opposite diagonal hatched red region). DBG and DRG data from Zirm et al. (2007) and Toft et al. (2007). (A color version of this figure is available in the online journal.)

$V - H$ and $I - H$ compared to Lyman break galaxies (LBGs) in the HDF, and suggests that one cannot create a DOG simply by adding an obscured AGN to a star-forming galaxy like an LBG. DRGs show greater overlap with the colors of DOGs, but few are as bright in H as the DOGs in our sample.

4.2.2. Non-parametric Classification Results

Nonparametric methods of characterizing galaxy morphology are known to require high S/N imaging to yield reliable results (Lotz et al. 2004). In the rest UV, where the DOGs are very faint, none of the 22 WFPC2 images and only six out of nine ACS images have the per pixel S/N necessary to compute R_p, G, M_{20}, and C. In the rest optical, however, DOGs are much brighter and 23 out of 31 NICMOS images have sufficient S/N. Table 5 presents the visual and nonparametric measures of DOG morphologies, including the per pixel S/N, R_p, G, M_{20}, and C values for the ACS/WFPC2 and NICMOS images.

In the left panel of Figure 7, we plot G as a function of M_{20} as measured in the rest UV for DOGs, a field galaxy sample, and simulated $r^{1/4}$ bulges and pure exponential disks (Lotz et al.

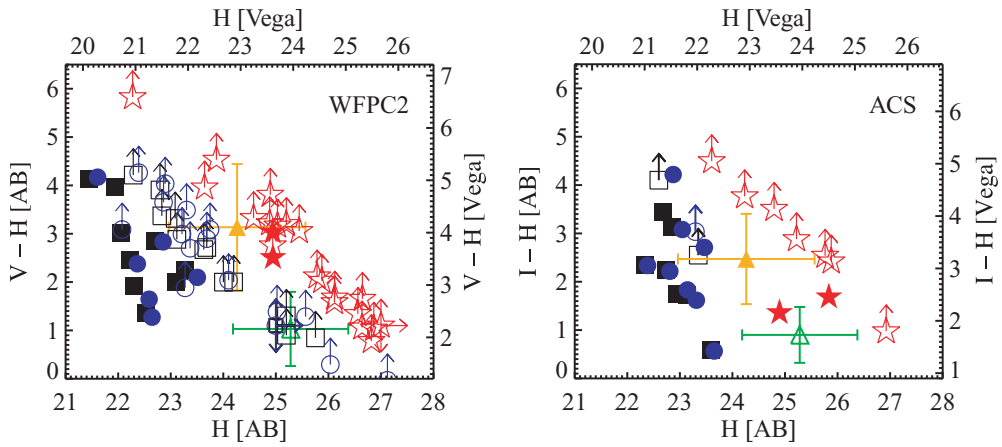

Figure 6. Color–magnitude diagram for DOGs, broken down into an extended component (unconstrained Sérsic profile) and an unresolved nuclear component (from TinyTim PSF). Left: $V - H$ vs. H for DOGs observed by WFPC2 (black squares). The extended component of each DOG is shown with a blue circle and the point source with a red star. Detections (Lower limits) are plotted with filled (open) symbols. Open green triangles show the median and 1σ dispersion in colors of high-z galaxies from the HDF-N (Papovich, personal communication and HDF-S (Labbé et al. 2003). The subset of these galaxies qualifying as DRGs are shown with a filled orange triangle. Right: $I - H$ vs. H for DOGs observed by ACS. Symbols are same as in left panel.

(A color version of this figure is available in the online journal.)

Table 5
Nonparametric Morphological Classifications

Source Name	ACS/WFPC2						NICMOS					
	Visual[a]	S/N	R_p ($''$)	G	M_{20}	C	Visual[a]	S/N	R_p ($''$)	G	M_{20}	C
SST24 J142538.2+351855	TFTT	...	...	...	...	...	Reg	...	...	...	...	...
SST24 J142622.0+345249	Irr	5.2	0.6	0.45	−0.8	3.6	Irr	3.0	0.5	0.44	−1.0	2.1
SST24 J142626.4+344731	Irr	...	...	...	...	...	Reg	...	...	...	...	...
SST24 J142644.3+333051	TFTT	...	...	...	...	...	Reg	10.7	0.3	0.56	−1.8	3.3
SST24 J142645.7+351901	TFTT	...	...	...	...	...	Irr	2.7	0.8	0.42	−0.7	4.3
SST24 J142648.9+332927	Irr	2.7	0.6	0.46	−0.8	4.9	Reg	2.6	0.6	0.50	−1.7	2.9
SST24 J142653.2+330220	Irr	2.2	0.8	0.42	−0.7	3.6	Reg	3.9	0.6	0.43	−1.2	2.2
SST24 J142804.1+332135	TFTT	...	...	...	...	...	TFTT	...	...	...	...	...
SST24 J142924.8+353320	TFTT	...	...	...	...	...	Irr	...	...	...	...	...
SST24 J142958.3+322615	Reg	...	...	...	...	...	Reg	3.8	0.5	0.46	−1.4	2.3
SST24 J143001.9+334538	TFTT	...	...	...	...	...	TFTT	...	...	...	...	...
SST24 J143025.7+342957	Reg	...	...	...	...	...	Reg	6.1	0.6	0.54	−1.7	2.9
SST24 J143102.2+325152	TFTT	...	...	...	...	...	TFTT	...	...	...	...	...
SST24 J143109.7+342802	TFTT	...	...	...	...	...	Irr	...	...	...	...	...
SST24 J143135.2+325456	TFTT	...	...	...	...	...	Irr	2.8	1.3	0.52	−2.5	4.7
SST24 J143225.3+334716	Irr	3.9	0.4	0.37	−1.6	2.4	Reg	5.1	0.5	0.50	−1.4	2.8
SST24 J143242.5+342232	TFTT	...	...	...	...	...	Irr	...	...	...	...	...
SST24 J143251.8+333536	TFTT	...	...	...	...	...	Reg	4.7	0.9	0.47	−1.7	2.7
SST24 J143312.7+342011	Irr	...	...	...	...	...	Reg	3.8	1.1	0.51	−1.4	3.3
SST24 J143325.8+333736	Reg	...	...	...	...	...	Reg	5.1	1.0	0.54	−1.9	−2.1[b]
SST24 J143358.0+332607	Reg	...	...	...	...	...	Reg	4.1	0.5	0.50	−1.4	3.1
SST24 J143447.7+330230	TFTT	...	...	...	...	...	Reg	4.3	0.5	0.46	−1.2	2.0
SST24 J143504.1+354743	TFTT	...	...	...	...	...	Reg	2.2	0.9	0.49	−0.9	−2.1[b]
SST24 J143508.4+334739	Irr	...	...	...	...	...	Reg	4.1	0.8	0.53	−1.2	2.9
SST24 J143520.7+340418	Reg	...	...	...	...	...	Reg	3.3	0.4	0.47	−0.9	3.3
SST24 J143523.9+330706	Reg	5.2	0.5	0.56	−1.2	2.8	Irr	6.3	0.4	0.47	−1.2	2.3
SST24 J143539.3+334159	TFTT	...	...	...	...	...	Reg	2.7	0.7	0.50	−1.7	3.4
SST24 J143545.1+342831	TFTT	...	...	...	...	...	Reg	4.6	0.6	0.55	−1.6	3.2
SST24 J143644.2+350627	TFTT	...	...	...	...	...	Reg	3.1	0.6	0.52	−1.7	2.7
SST24 J143725.1+341502	TFTT	...	...	...	...	...	Reg	2.5	0.9	0.52	−2.1	3.7
SST24 J143808.3+341016	Irr	2.3	1.3	0.44	−0.9	3.6	Irr	2.3	1.0	0.48	−1.6	3.2

Notes.
[a] Mode of visual classification. Italics indicate multiple users disagreed with the mode.
[b] Negative C value indicates r_{20} was too small to be measured accurately.

2006). None of the DOGs fall within the pure exponential disk- or $r^{1/4}$ bulge-dominated regime. The field galaxy population is composed of sources identified within the ACS FOVs and is selected to span the same magnitude range as the DOGs in our sample. We use our NDWFS data to apply color cuts in $B_W - R$ and $R - I$ space in order to remove objects with colors typical of

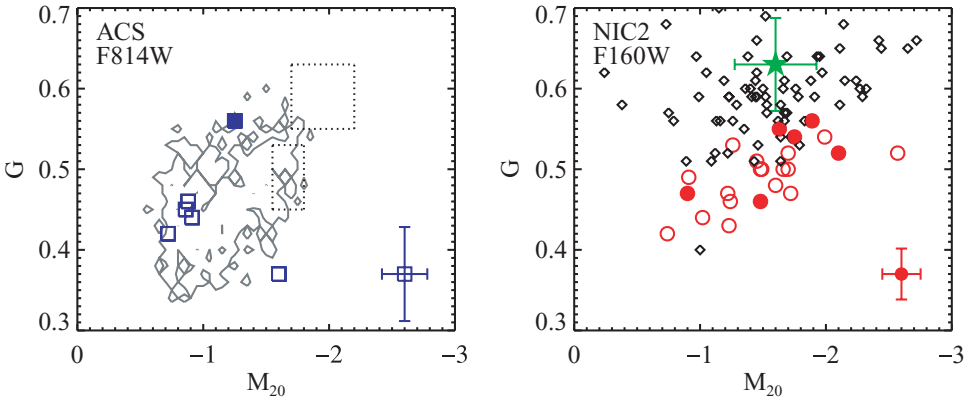

Figure 7. Gini coefficient vs. M_{20}. Left: morphological measures from ACS/F814W images of DOGs (blue squares) and field galaxies (grey solid contours, see text). Representative error bars in the lower right corner include uncertainties due both to low S/N and low spatial resolution and are estimated using a method similar to that in Lotz et al. (2004). Filled symbols have greater than 20% point-source contribution. Top and bottom dotted boxes show where simulated face-on bulges and disks lie, respectively (Lotz et al. 2006). Right: same plot but showing results from NIC2/F160W images of DOGs (red circles), HDF-N LBGs (filled green star) and a sample of local ULIRGs (black diamonds) (Lotz et al. 2004).

(A color version of this figure is available in the online journal.)

$z < 0.7$ sources. The morphologies of this field galaxy sample are represented with gray contours. Four out of six DOGs lie in the lower left corner of the plot, with low G and high M_{20} values indicating irregular, diffuse morphologies. In general, low G and high M_{20} values are indicative of dust-enshrouded stellar populations, where obscuration by dust causes a galaxy to appear very clumpy with flux distributed among many pixels (Lotz et al. 2008).

One object (SST24 J143523.9+330706, panel 27 in Figure 3) has a higher G and lower M_{20} value than nearly all of the field galaxies. This is the same object that shows a stronger point-source contribution in the rest UV than the rest optical. Visual inspection of this object's cutout image reveals an extended feature fading toward the southeast that is present in both the rest UV and rest optical. It appears that the central activity in this source is not quite as obscured as in other DOGs, but it is not yet clear why this is the case.

The right panel in Figure 7 shows G and M_{20} values as measured in the rest optical for DOGs as well as LBGs in the HDF-N and a sample of local ($z < 0.1$) ULIRGs (Lotz et al. 2004). DOGs shift to more typical morphological parameters in the rest optical compared to the rest UV, but they are offset from the parameter space occupied by LBGs and local ULIRGs. The median G and M_{20} values for DOGs are 0.49 and −1.24, respectively, while for LBGs they are 0.63 and −1.6, and for local ULIRGs they are 0.59 and −1.5. Part of the difference in G and M_{20} compared to LBGs may be that LBGs are more compact, and hence less resolved. The offset to lower G values in DOGs compared to local ULIRGs is remarkable and indicates that either different mechanisms are involved in creating these two populations, or they represent different stages in the evolution of massive galaxies. We note that the ULIRG sample has comparable S/N as the DOGs studied here, and that the rest-frame wavelength of both samples is similar (∼7000 Å versus ∼5300 Å, respectively). While there is a greater relative difference in the spatial resolution of the two samples (≈0.2 kpc pix^{-1} versus (≈0.6 kpc pix^{-1}, respectively), Lotz et al. (2004) found that systematic offsets at these resolutions should be on the order of 20% or less for C and M_{20} and less than 10% for G. Therefore, the difference in G cannot be explained by spatial-resolution effects alone.

As a qualitative consistency check, we examined R-band images of a sample of 56 ULIRGs from Murphy et al. (1996) and determined that 20 (35%) have double nuclei with nuclear separations larger than 2.3 kpc, approximately the resolution limit of our NIC2 images. In comparison, only one DOG has two well-detected, distinct nuclei and three or four have low S/N components separated by 0.″5 (≈4 kpc), implying that at most 16% of the DOGs in our sample have multiple nuclei with separations larger than 2.3 kpc. This result is qualitatively consistent with the differences seen in G between local ULIRGs and DOGs. An important caveat with this analysis is that our sample of DOGs is dominated by power-law sources, while the ULIRG sample has a variety of rest-frame NIR SED shapes. For reference, we measured the G and M_{20} values of a well-detected, non-DOG point source (S/N per pixel of 18) in one of our NIC2 images, and found values of 0.62 and −1.7, respectively. The DOG whose morphology is dominated by a point source (see panel 31 in Figure 3) has a lower G value (0.56), but almost the same M_{20} (−1.8). This may be an indication that this DOG contains an underlying extended component, but the data are not conclusive.

5. DISCUSSION

5.1. Dust and Stellar Mass Estimates

Here we estimate some of the intrinsic properties of DOGs including lower limits on their reddening (A_V), dust and gas masses, and stellar masses. To do this, we use Simple Stellar Population (SSP) template SEDs from the Bruzual & Charlot (2003) population synthesis library with ages spaced logarithmically from 10 Myr up to 1 Gyr, as well as the median QSO template from Elvis et al. (1994). All models used here have solar metallicity, a Chabrier IMF over the mass range 0.1–100 $M_\odot$ (Chabrier 2003), and use the Padova 1994 evolutionary tracks (Girardi et al. 1996). The reddening law used is a combination of that from Calzetti et al. (2000) and longer wavelength estimates from Draine (2003), and assumes the case of a dust screen in front of the emitting source in order to derive a firm lower limit on A_V.

For each DOG, we estimate A_V needed as a function of age by determining the amount of extinction necessary to redden the given SSP template such that it reproduces the observed $V - H$

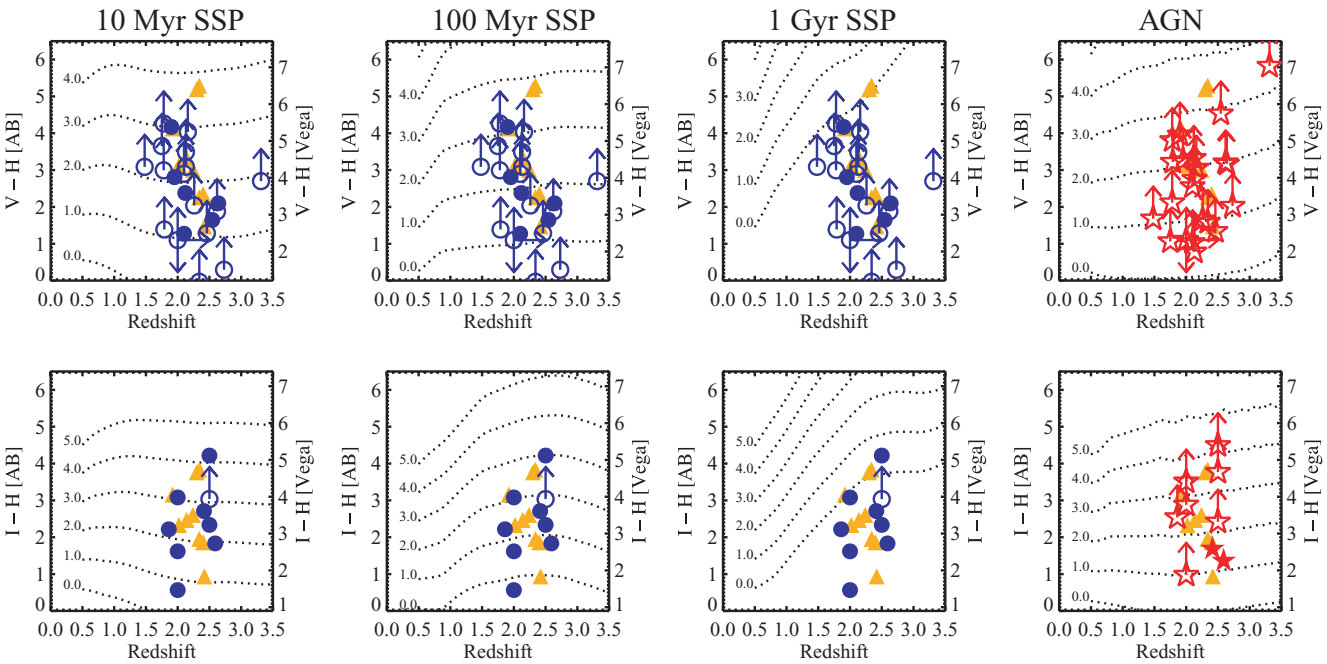

Figure 8. $V-H$ (top row) and $I-H$ (bottom row) as a function of spectroscopic redshift for each DOG. The first three columns show the colors of the extended component, while the fourth column shows the colors of the unresolved component (filled symbols are detections, open symbols are lower limits). Filled orange triangles represent DRGs in the HDF-S. Dotted lines trace the evolution of colors with redshift of reddened simple stellar population models from Bruzual & Charlot (2003) with solar metallicity, a Chabrier IMF and at ages of 10 Myr, 100 Myr, and 1 Gyr (three columns on left), as well as of the median QSO template from Elvis et al. (1994).

(A color version of this figure is available in the online journal.)

or $I-H$ color. The process is illustrated in Figure 8. Each panel shows the colors of DOGs in our sample as a function of redshift. Blue circles represent the extended component and red stars show the point source component of each DOG, as described in Section 4.2.1. Dotted lines show the expected colors of the SSP templates for varying amounts of extinction. Even with no extinction ($A_V = 0$), the oldest SSP templates are too red to reproduce the colors exhibited by DOGs. The quasi-stellar object (QSO) templates, on the other hand, require large A_V values in order to match the DOG nuclear colors.

We use the relation from Bohlin et al. (1978) to convert A_V to the total column density of hydrogen atoms and molecules, $N_{\rm H}$. For the 100 Myr SSP, the column densities range from 3×10^{20}–6×10^{21} cm^{-2}, with a median $N_{\rm H}$ of 3×10^{21} cm^{-2}. If we assume the dust is distributed in a spherical shell around the source with radius equal to the effective radius, then we can place a lower limit on the dust mass:

$$M_{\rm dust} \geqslant \frac{1}{f_{\rm gd}}\mu_{\rm p} N_{\rm H} \times 4\pi R_{\rm eff}^2. \quad (1)$$

Here, $f_{\rm gd}$ is the gas-to-dust mass ratio, and $\mu_{\rm p}$ is the mean molecular weight of the gas, which we take to be $1.6m_{\rm p}$, where $m_{\rm p}$ is the mass of a proton. We adopt the average gas-to-dust mass ratio of 120 measured for the nuclear regions of local ULIRGs by Wilson et al. (2008). We find dust mass lower limits ranging from 2×10^5–$6\times10^7\,M_\odot$, with a median of $9\times10^6\,M_\odot$ for a 100 Myr SSP.

A complementary method of estimating the dust mass is based on measurements of optically thin sub-mm emission. Because sub-mm photometry for the DOGs in our sample is currently unavailable, we extrapolate from the 24 μm flux density measurement. We used the Mrk231 template to determine the extrapolated 850 μm flux density, F_{850}. Using a template SED of a galaxy with colder dust such as Arp220 would increase the inferred 850 μm flux. We follow Hughes et al. (1997) and estimate the dust mass using

$$M_{\rm dust} = \frac{1}{1+z}\frac{F_{850}d_{\rm L}^2}{\kappa_{\rm d}B(\nu, T_{\rm d})}, \quad (2)$$

where $d_{\rm L}$ is the luminosity distance, $\kappa_{\rm d}$ is the rest-frequency mass absorption coefficient, and $B(\nu, T)$ is the value of the modified blackbody function ($\beta = 1.5$) at the rest frequency ν and a temperature T. The appropriate $\kappa_{\rm d}$ value is interpolated from Draine (2003), with typical values being 5 cm^2 g^{-1}. There is at least a factor of 2 uncertainty in this quantity. We have assumed relatively hot dust ($T_{\rm d} = 75$ K), since we expect AGN heating to play an important role in this sample of DOGs (a dust temperature of 50 K would increase the inferred dust mass by an additional factor of $\approx$1.5). Using this method, we find dust masses of 8×10^7–$6\times10^8\,M_\odot$, with the median dust mass being $1.6\times10^8\,M_\odot$. This is a factor of nearly 20 larger than the median dust mass inferred from the measurements of A_V. This might be expected, given that many of the dust masses based on A_V are lower limits, while the dust masses based on theb 24 μm emission may be overestimates if $T_{\rm d} > 75$ K. On the other hand, this difference may be suggesting that the dust causing the average UV extinction of the extended galaxy component is not the same dust that is causing the thermal emission.

We use the SSP templates to estimate the stellar mass in each DOG. This is computed by reddening each SSP template to match the observed color of the DOG at the appropriate redshift. We then scale the redshifted, reddened template to match the observed H-band photometry. Since the Bruzual & Charlot (2003) models are normalized to a stellar mass of 1 $M_\odot$, this scaling factor represents the stellar mass of the DOG.

In Figure 9, we show the stellar mass of each DOG as a function of age as well as the distribution of stellar masses

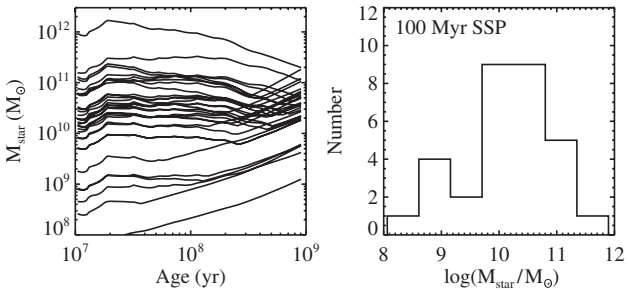

Figure 9. Left: stellar mass as a function of SSP age for the DOGs. Right: distribution of stellar masses at an age of 100 Myr.

assuming a 100 Myr SSP model. As stellar populations age, their colors naturally redden, and so less extinction is needed to reproduce the observed colors of the DOGs. For most DOGs, ages greater than ∼300 Myr require A_V values less than zero and are unphysical. Meanwhile, at younger ages, lower mass-to-light ratios are balanced by the need for greater extinction to match the observed colors. As a result, the inferred stellar masses are relatively constant to within a factor of a few for ages less than 300 Myr. We note that these mass estimates are lower limits because (1) the amount of extinction is a lower limit, especially when there is no detection in the *V*- or *I*-band image, and (2) our extinction estimate does not take into account gray extinction. For an age of 100 Myr, the stellar masses range from 2×10^8–1×10^{12} $M_\odot$, with the median mass being 3.3×10^{11} $M_\odot$.

We use our dust mass estimates inferred from the 24 μm flux densities and a gas-to-dust mass ratio of 120 (Wilson et al. 2008) to obtain an upper limit on the gas masses. This leads to gas masses of 1–7×10^{10} $M_\odot$, with a median gas mass of 2×10^{10}. If we assume a closed-box model and an exponential star-formation history, then we can write $M_{\rm gas} + M_{\rm dust} = M_{\rm tot}\exp(-t/t_0)$, where $M_{\rm tot}$ is the sum of the gas, dust, and stellar masses. The stellar mass is then given by $M_{\rm star} = M_{\rm tot}(1 - \exp(-t/t_0))$, which implies

$$\frac{t}{t_0} = \ln\frac{M_{\rm tot}}{M_{\rm gas} + M_{\rm dust}}. \quad (3)$$

This quantity represents the fractional lifetime (in units of the scale time for our exponential star-formation rate assumption) of each DOG. Larger values of t/t_0 indicate more evolved systems, as more of the gas has been converted to stars. Our values of t/t_0 represent lower limits on the actual values, because our stellar masses are underestimated and our gas masses are based on our 24 μm flux densities, which likely overestimates the true mass of gas. We find t/t_0 lower limits ranging from 0.02 to 3.3, with a median lower limit of 0.9. This result implies that in half of the DOGs in our sample, at least 90% of one exponential timescale's worth of star formation has occurred. The "oldest" DOG in our sample has gone through more than three exponential timescales of evolution. However, we caution that the "youngest" DOGs from this line of analysis are uniformly associated with sources where the dust extinction is most likely underestimated, thereby causing an additional underestimate in the stellar mass and the associated t/t_0 value. In Table 6, we present the dust and stellar masses derived in this section, as well as our measure of the lower limit on the fractional lifetime, t/t_0.

Table 6
DOG Mass Estimates

DOG	$M_{\rm dust}$[a] (10^7 $M_\odot$)	$M_{\rm star}$[b] (10^{10} $M_\odot$)	t/t_0[c]
SST24 J142538.2+351855	0.8−11	0.8	0.5
SST24 J142622.0+345249	0.5−13	0.4	0.2
SST24 J142626.4+344731	2.0−15	2.9	1.0
SST24 J142644.3+333051	0.3−32	11.0	1.4
SST24 J142645.7+351901	5.2−13	5.1	1.5
SST24 J142648.9+332927	0.7−24	1.3	0.4
SST24 J142653.2+330220	2.9−8	3.8	1.6
SST24 J142804.1+332135	2.8−12	0.02	0.02
SST24 J142924.8+353320	0.2−16	0.08	0.04
SST24 J142958.3+322615	0.5−19	2.0	0.6
SST24 J143001.9+334538	0.1−60	0.1	0.02
SST24 J143025.7+342957	0.3−37	2.8	0.5
SST24 J143102.2+325152	—	—	—
SST24 J143109.7+342802	7.7−13	2.2	0.9
SST24 J143135.2+325456	4.9−29	4.5	0.8
SST24 J143225.3+334716	1.7−13	9.6	2.0
SST24 J143242.5+342232	4.7−11	13.0	2.4
SST24 J143251.8+333536	3.5−9	13.0	2.6
SST24 J143312.7+342011	3.6−23	4.9	1.0
SST24 J143325.8+333736	3.8−17	32.0	2.8
SST24 J143358.0+332607	1.1−15	6.6	1.5
SST24 J143447.7+330230	0.9−18	2.4	0.7
SST24 J143504.1+354743	5.1−16	5.4	1.3
SST24 J143508.4+334739	0.4−31	1.4	0.3
SST24 J143520.7+340418	0.1−16	0.1	0.05
SST24 J143523.9+330706	0.5−16	3.3	1.0
SST24 J143539.3+334159	1.1−43	2.0	0.3
SST24 J143545.1+342831	2.5−30	95.0	3.3
SST24 J143644.2+350627	1.0−22	3.7	0.9
SST24 J143725.1+341502	2.4−22	13.0	1.8
SST24 J143808.3+341016	1.1−26	12.0	1.6

Notes.
[a] Mass range reflects estimates based on A_V and 24 μm flux density.
[b] Stellar mass estimates represent lower limits on true stellar mass.
[c] t/t_0 estimates are lower limits based on 24 μm dust masses.

5.2. Comparison to Other High Redshift Galaxy Populations

It is important to understand how DOGs are related to other populations of high-*z* galaxies that have been studied in the literature. Here, we compare the morphological properties of the DOGs with some of these high-redshift galaxy populations and find that DOG morphologies are distinct from the bulk of LBGs and quiescent high-*z* galaxies, but are similar to SMGs as well as active DRGs and the extreme subset of faint, diffuse LBGs.

5.2.1. Sub-mm Galaxies

SMGs are a particularly interesting population of galaxies to compare with DOGs. First identified by blind sub-mm surveys with the Submillimetre Common User Bolometer Array (SCUBA Holland et al. 1999), SMGs may represent an important, short-lived, and very active phase in the evolution of the most massive galaxies. Their redshift distribution, number density, and clustering properties are similar to DOGs (Chapman et al. 2005; Dey et al. 2008; Blain et al. 2004; Brodwin et al. 2008). However, a sample of DOGs detected at 70 μm or 160 μm by *Spitzer*/MIPS tends to show warmer colors (i.e., smaller 70/24 μm or 160/24 μm flux density ratios) compared to SMGs (Tyler et al. submitted). One speculative scenario that may serve as a possible explanation for this behavior is that these two galaxy populations are linked in an evolutionary sense: SMGs represent a cold dust, star-formation dominated stage in the formation of massive galaxies that may

precede the DOG phase, when the feedback from the growth of a central black hole has heated the surrounding gas and dust, thereby quenching star formation and shifting the peak of the SED to shorter wavelengths.

If this scenario is correct, then we expect to see major mergers dominate the morphologies of SMGs, while DOGs should show more relaxed morphologies typical of the final merger stage before the remnant. Conselice et al. (2003) analyzed Space Telescope Imaging Spectrograph (STIS) rest-frame UV data of a sample of 11 SMGs at $z \sim 2$–3 using the CAS system, and found evidence suggesting a major merger fraction of between 40% and 80%. Although we do not have the S/N in our images to measure A reliably (and thereby determine a major merger fraction in a similar manner), the low G and high M_{20} values we have measured imply diffuse, irregular systems where the light is spread into multiple components rather than two separate components. If the DOGs were predominantly major mergers, we would expect our sample to have higher G values. Instead, the low G values we find suggest that we may be looking at the dusty remnant of a major merger, where there are many highly obscured components near each other. However, we caution that dust can have a strong effect on the measured G value in the rest UV, such that even major mergers might yield lower G values.

The rest-UV morphologies of SMGs have also been analyzed in the GOODS-N field, where a SCUBA supermap exists and has been used to identify robust sub-mm detections (Borys et al. 2003). A sample of 12 sources in the redshift range 1.7–4.0 (comparable to the DOGs) were studied by Pope et al. (2005), who computed concentration and asymmetry values, finding C to be in the range of 2–3.3 and A to be dominated by noise, with the exception of two objects (one is very compact and the other is clearly asymmetric). The comments associated with many of these sources are "faint" and "diffuse," suggesting that there is large-scale dust obscuration in these systems. This is qualitatively similar to what is seen in many of the DOGs, suggesting that there is some overlap between the two samples.

SMGs have not yet been characterized in terms of G or M_{20}, so direct comparisons based on these quantities are not possible at this time. However, we can compare the sizes of these systems directly via the Petrosian radius. In the rest UV, the DOGs range in size from $R_p \sim 0\farcs5$ to $1\farcs5$, while SMGs range in size from $0\farcs5$ to $2\farcs5$. Indeed, a two-sided KS test reveals that there is only a 5% chance that they are drawn from the same parent distribution. This suggests that while there are similarities between SMGs and DOGs, SMGs tend to be slightly larger than DOGs. This is consistent with the major merger hypothesis in which DOGs are in a more evolved state where dynamical friction has caused individual components to fall toward the center of mass. However, we caution that this result in itself does not provide evidence for DOGs originating from major mergers. Objects moving at $\sim$100 km s^{-1} will traverse 8 kpc in $\lesssim$100 Myr. Simulations of major mergers predict a phase of intense star formation and central black hole growth that lasts of order this timescale, indicating that the size differences are at least consistent with the scenario outlined above (Hopkins et al. 2008).

Finally, the ratio of the stellar mass to the gas mass holds potential for comparing the evolutionary states of SMGs and DOGs. The ideal comparison study would include statistically significant samples of both populations of galaxies for a range of observed properties such as 24 μm emission, bolometric luminosity, space density, etc. Unfortunately, such samples do not currently exist—mainly due to a combination of the limitations of current instrumentation and the fact that these are relatively recently discovered populations of galaxies. While CO linewidths and emission strengths have found gas mass estimates for a handful of SMGs, no such measurements have been published for DOGs. The gas mass estimates for SMGs are typically $\sim 5 \times 10^{10}\ M_\odot$ (Greve et al. 2005; Tacconi et al. 2006, 2008). A number of efforts have been directed at determining the stellar masses of SMGs using SED-fitting algorithms. Average stellar mass values are in the range of 3–6 $\times\ 10^{11}\ M_\odot$ (Borys et al. 2005; Dye et al. 2008). However, when we employ our method of determining the stellar mass (in this case using the $R - K$ color to determine the optimal A_V value for a given SSP and age) using the photometry presented in those papers, we find average stellar masses of $\sim 7 \times 10^{10}\ M_\odot$. These estimates increase by a factor of $\approx$2, if instead of a Chabrier IMF we use a Salpeter IMF (as was done by the previous authors for SMGs). However, this still leaves us a factor of $\approx$2 short of the mass estimates provided in the papers described above. In order to compare DOG stellar masses with SMGs consistently, we adopt the lower stellar mass values that we derive for SMGs. In this case, the median t/t_0 value for SMGs becomes $\approx$1.1, which is much closer to the median lower limit value of 0.9 found for the DOGs in Section 5.1.

The large uncertainty inherent in the process of estimating dust and gas masses based on 24 μm photometry or rest-frame optical A_V measurements currently prevents a strong conclusion being made regarding the evolutionary status using this line of analysis. However, the morphological evidence is suggestive—although not conclusive—of an evolutionary link between the two populations with SMGs serving as the less evolved precursor to the DOG phase.

5.2.2. *Star-forming Galaxies*

A number of selection criteria have been used to identify normal star-forming galaxies at high redshift. Two of these are the LBG dropout (Madau et al. 1996; Steidel et al. 1996) and BzK (Daddi et al. 2004) techniques. A direct comparison to our work can be made with a sample of LBGs and emission line galaxies in the GOODS-N field studied by Lotz et al. (2006). These authors compared G, M_{20}, and C values between their sample of 82 $z \sim 4$ LBGs and 55 $z \sim 1.5$ emission line galaxies. In the LBG sample, they found a major-merger fraction of $\sim$10–25% (defined by $M_{20} \geqslant -1.1$) and a bulge-dominated fraction of $\sim$ 30% ($G \geqslant 0.55$, $M_{20} < -1.6$). The remainder of the LBGs had G and M_{20} values larger than what is typical for normal galaxies, suggesting active star-formation or a recent merger event. The low-z emission-line sample showed a similar major merger fraction but fewer bulge-dominated systems. It is remarkable then that so few of the DOGs have G and M_{20} values typical of bulge-dominated systems, even in the rest optical, despite their luminosity. Furthermore, four out of six DOGs with measurable morphologies in the rest UV have high M_{20} and low G values that are typical of dusty, irregular systems. This may be an indication of kpc scale dust obscuration, which can bias the G and M_{20} values away from the bulge-dominated regime.

A morphological study of LBGs in GOODS-N by Ravindranath et al. (2006) found axial ratios skewed toward lower values for galaxies at $z > 3$, suggesting high-z LBGs are dominated by edge-on morphologies. In contrast, only one DOG has an axial ratio less than 0.35, indicating that if these sources are disk galaxies, then some selection mechanism must be in place that favors observing DOGs in face-on orientations.

Meanwhile, results from numerical simulations of galaxy mergers indicate that remnants end up with axial ratios between 0.5 and 1.0, depending on the viewing angle (Novak et al. 2006). 21 DOGs satisfy this axial ratio criterion, but the median value in our data set is ≈0.5. This suggests that either DOGs represent a phase prior to the final remnant stage or they are formed by some other process.

Recently, Law et al. (2007) have used GOODS data to analyze morphologies of 216 LBGs and compare them with other high-z galaxy populations. They found significant overlap between the LBGs and BzKs, indicating that the optical and NIR selection criteria are identifying similar galaxies. While these authors performed a nonparametric morphological analysis, direct comparison between our work and theirs is difficult because (a) they assign pixels to each galaxy based on an isophotal surface brightness criterion rather than the elliptical Petrosian radius as we have done, and (b) they create their own parameter to describe the multiplicity (Ψ) of each galaxy, rather than using M_{20}. Nevertheless, there are some apparent differences between the DOGs and LBGs from the Law et al. (2007) study. While the LBGs span the full range of G values in the rest UV, the DOGs tend to be low G objects. Furthermore, though LBGs span a wide range in G, they are preferentially found to have low Ψ values, implying a small number of distinct components. On the other hand, the DOGs have high M_{20} values, suggesting that the multi-component structure is commonplace. Law et al. (2007) note a correlation in their plot of G as a function of Ψ in the sense that objects with many components (large Ψ) tend to be fainter and more nebulous (low G). DOGs resemble this extreme subset of faint diffuse LBGs, but appear highly morphologically distinct from the vast majority of the LBG population.

5.2.3. Passively Evolving Galaxies

As mentioned above, the BzK method can be used to identify high-z passively evolving galaxies. This photometric color cut has been used in the Hubble Ultra Deep Field (UDF) to generate a sample of seven luminous early-type galaxies at $z = 1.39$–2.47 (Daddi et al. 2005). These authors studied the i and z band morphologies of all seven objects with both parametric (Sérsic profile fitting) and nonparametric (concentration and asymmetry) methods. They found fairly large Sérsic indices ($n \sim 3$) and small effective radii ($r_{\rm eff} \lesssim 1$ kpc), typical of E/S0 galaxies. In contrast, the best-fit Sérsic profile for DOGs has smaller n values more typical of exponential disks (median $n = 0.9$) and larger effective radii ($R_{\rm eff} \sim 1$–6 kpc). Moreover, the passive BzK galaxies have $C > 2.6$ and $A < 0.2$, consistent with early-type systems. In the rest optical, DOGs tend to show lower C values (S/N is not sufficient to measure A), consistent with an exponential profile. Along with the low G and high M_{20} values that are measured for the DOGs, these morphology results suggest that DOGs and passively evolving high-z galaxies are distinct populations, either because they represent different stages of evolution or because they have different formation mechanisms.

5.2.4. Distant Red Galaxies

Another population of high-z galaxies is the so-called Distant Red Galaxies (DRGs). Identified via deep NIR imaging, these objects were first postulated to be the reddened descendents of LBGs (Franx et al. 2003). Subsequent studies of DRGs in the Extended Growth Strip (EGS) show a wide variety of shapes, with 57% appearing visually as elliptical/compact, 7% as edge-on disks, and the remainder as peculiar/irregular galaxies (Conselice et al. 2007). The low-redshift DRGs ($z < 1.4$) have CAS values typical of nearby normal galaxies. The higher z DRGs visually classified as elliptical/compact have higher C values, similar to what is seen locally in massive ellipticals and in the BzK samples. Meanwhile, Law et al. (2007) examined DRGs in the GOODS-N field that did not overlap with the BX or BM LBG color criteria and found that this population of galaxies was substantially fainter and more diffuse than either the star-forming BzKs or the LBGs. They note that this is the behavior one expects from dusty, IR-bright galaxies. The faint, diffuse nature of these objects is reminiscent of the DOGs, and it is possible that there is significant overlap between these two populations.

Previous work using rest-frame UV–NIR SEDs has separated actively star-forming DRGs (sDRGs) from quiescent ones (qDRGs) (Zirm et al. 2007; Toft et al. 2007). Examination of the morphological differences between these two populations has revealed a correlation between size and star-formation activity in the sense that qDRGs are all very small ($R_{\rm eff} \lesssim 1$ kpc), while sDRGs span a larger range in size ($R_{\rm eff} \sim 1$–10 kpc). As is shown in the right panel of Figure 5, DOGs appear very similar to sDRGs in terms of their sizes. This is consistent with the qualitative similarity between sDRGs and DOGs, described in the preceding paragraph and suggests that there is an extensive overlap between these two populations.

5.3. Implications for the Evolution of the Most Massive Galaxies

In the local universe, there has been evidence for some time that warm dust-dominated ULIRGs may represent a transition stage between cold ULIRGs and optically luminous quasars (Sanders et al. 1988b). If this scenario holds at high redshift, then there is a natural explanation for the observations based on the selection criteria alone: objects selected at long wavelengths (i.e., SMGs) are preferentially cold-dust-dominated systems and represent the "cold ULIRG" phase, whereas objects selected at 24 μm (i.e., DOGs) are dominated by warmer dust and represent the transition phase en route to the optically luminous quasar. As time progresses and the quasar fades in luminosity, the compact, quiescent, elliptical galaxy remnant becomes visible (i.e., quiescent BzKs and DRGs).

Again referring to the local universe for guidance, if the triggering mechanism for this activity is a major merger (Sanders et al. 1988a), then we should expect to see a trend in relaxation and size, where the initial stage shows the largest sizes and least relaxation, and the end product is a relaxed, compact system. This picture is apparently consistent with our data, as DOGs tend to be smaller than SMGs, but larger than quiescent DRGs or BzK galaxies. Furthermore, SMGs frequently exhibit signs of major merger activity, whereas passively evolving systems at high z are very compact with large Sérsic indices. DOGs appear to be intermediate stage objects that typically do not show signs of major mergers, but nonetheless have morphologies indicating they are more dynamically relaxed than SMGs but less than the quiescent systems.

It is important to emphasize that while our morphological results are consistent with the hypothesis that DOGs act as a transition phase in the process of creating a massive galaxy via a major merger, the morphological information currently available is not sufficient to exclude the possibility that DOGs are created by some other process such as minor merging (for example, minor mergers have the potential to increase size

temporarily), or are simply dusty galaxies hosting a powerful, obscured AGN.

Our analysis of the stellar, dust, and gas masses of DOGs currently does not provide compelling evidence to place them within an evolutionary scheme with respect to other massive proto-galaxy candidates such as SMGs. Additional data are needed before conclusive statements can be made based on mass estimates such as these.

6. CONCLUSIONS

We have analyzed the morphologies of 31 Dust Obscured Galaxies (DOGs) at $z \approx 2$ from the Boötes field, using data from *HST* ACS/WFPC2 and NICMOS. Our findings are summarized below.

1. Although these sources were selected to have mid-IR signatures of AGN, we detect spatially resolved emission at rest-frame UV and/or rest-frame optical wavelengths for all but one of the 31 targets.
2. Using a three-component model in GALFIT (sky + PSF + Sérsic profile), we measure significant unresolved components in 28 out of 31 DOGs in the rest optical, and the median point-source fraction is 0.13. Only 10 DOGs have measurable unresolved components in the rest UV.
3. The median Sérsic index is 0.9, indicating that disk-like profiles are preferred to bulge-like ones. On the other hand, very few DOG-extended components have small axial ratios, indicating that if DOGs are predominantly a population of normal, disk-like galaxies (with an obscured AGN producing the 24 μm flux), then some selection mechanism(s) must be in place that favors face-on rather than edge-on orientations.
4. DOGs in our sample have effective radii of 1–5 kpc, which places them between SMGs and quiescent DRGs or BzK galaxies. If DOGs are formed by a major merger, this trend in sizes is consistent with them acting as a transition stage in the evolution of massive galaxies. If DOG activity is triggered by some other process, such as a minor merger or a dusty AGN in a normal galaxy, then interpretation of this size trend is not as clear.
5. In the rest optical, DOGs have lower G values than local ULIRGs (median values of 0.49 and 0.59, respectively). This might be expected if DOGs represent a subsequent stage in the merging process (just before coalescence), but might also be expected if the galaxies are not disturbed by a major merger.
6. Simple stellar population modeling reveals that old (>300 Myr) single-burst stellar populations are redder than most DOGs and thus ruled out. If 100 Myr old SSPs are appropriate, then DOGs require substantial amounts of extinction to produce the observed red colors, with $A_V = 0.2$–3. This provides a lower bound on the median dust mass of $10^7\ M_\odot$. An upper bound is obtained by extrapolating the 24 μm flux density to 850 μm and is found to have a median value of $1.5 \times 10^8\ M_\odot$. We find a median stellar mass lower limit of $3 \times 10^{10}\ M_\odot$, which is relatively insensitive to age to within a factor of a few.

This work is based in part on observations made with the *Spitzer Space Telescope*, which is operated by the Jet Propulsion Laboratory, California Institute of Technology under NASA contract 1407. We are grateful to the expert assistance of the staff Kitt Peak National Observatory, where the Boötes field observations of the NDWFS were obtained. The authors thank NOAO for supporting the NOAO Deep Wide-Field Survey. In particular, we thank Jenna Claver, Lindsey Davis, Alyson Ford, Emma Hogan, Tod Lauer, Lissa Miller, Erin Ryan, Glenn Tiede and Frank Valdes for their able assistance with the NDWFS data. We also thank the staff of the W. M. Keck Observatory, where some of the galaxy redshifts were obtained.

R.S.B. gratefully acknowledges financial assistance from HST grant GO10890, without which this research would not have been possible. Support for Program number HST-GO10890 was provided by NASA through a grant from the Space Telescope Science Institute, which is operated by the Association of Universities for Research in Astronomy, Incorporated, under NASA contract NAS5-26555. The research activities of A.D. and B.T.J. are supported by NOAO, which is operated by the Association of Universities for Research in Astronomy (AURA) under a cooperative agreement with the National Science Foundation. Support for E. Le Floc'h was provided by NASA through the *Spitzer* Space Telescope Fellowship Program.

REFERENCES

Abraham, R. G., Valdes, F., Yee, H. K. C., & van den Bergh, S. 1994, ApJ, 432, 75
Abraham, R. G., van den Bergh, S., & Nair, P. 2003, ApJ, 588, 218
Bertin, E., & Arnouts, S. 1996, A&AS, 117, 393
Blain, A. W., Chapman, S. C., Smail, I., & Ivison, R. 2004, ApJ, 611, 725
Bohlin, R. C., Savage, B. D., & Drake, J. F. 1978, ApJ, 224, 132
Borys, C., Chapman, S., Halpern, M., & Scott, D. 2003, MNRAS, 344, 385
Borys, C., Smail, I., Chapman, S. C., Blain, A. W., Alexander, D. M., & Ivison, R. J. 2005, ApJ, 635, 853
Brand, K., et al. 2006, ApJ, 641, 140
Brand, K., et al. 2007, ApJ, 663, 204
Brand, K., et al. 2008, ApJ, 680, 119
Brodwin, M., et al. 2008, ApJ, 687, L65
Bruzual, G., & Charlot, S. 2003, MNRAS, 344, 1000
Calzetti, D., Armus, L., Bohlin, R. C., Kinney, A. L., Koornneef, J., & Storchi-Bergmann, T. 2000, ApJ, 533, 682
Chabrier, G. 2003, PASP, 115, 763
Chapman, S. C., Blain, A. W., Smail, I., & Ivison, R. J. 2005, ApJ, 622, 772
Conselice, C. J. 2003, ApJS, 147, 1
Conselice, C. J., Chapman, S. C., & Windhorst, R. A. 2003, ApJ, 596, L5
Conselice, C. J., Rajgor, S., & Myers, R. 2008, MNRAS, 386, 909
Conselice, C. J., et al. 2007, ApJ, 660, L55
Daddi, E., Cimatti, A., Renzini, A., Fontana, A., Mignoli, M., Pozzetti, L., Tozzi, P., & Zamorani, G. 2004, ApJ, 617, 746
Daddi, E., et al. 2005, ApJ, 626, 680
Dasyra, K. M., Yan, L., Helou, G., Surace, J., Sajina, A., & Colbert, J. 2008, ApJ, 680, 232
Dey, A., et al. 2008, ApJ, 677, 943
Donley, J. L., Rieke, G. H., Pérez-González, P. G., Rigby, J. R., & Alonso-Herrero, A. 2007, ApJ, 660, 167
Draine, B. T. 2003, ARA&A, 41, 241
Dye, S., et al. 2008, MNRAS, 386, 1107
Eisenhardt, P. R., et al. 2004, ApJS, 154, 48
Elvis, M., et al. 1994, ApJS, 95, 1
Faber, S. M., et al. 2003, in SPIE Conf., 4841, Instrument Design and Performance for Optical/Infrared Ground-based Telescopes, ed. M. Iye & A. F. M. Moorwood (Bellingham, WA: SPIE), 1657
Fiore, F., et al. 2008, ApJ, 672, 94
Ford, H. C., et al. 1998, in SPIE Conf., 3356, Space Telescopes and Instruments: V, ed. P. Y. Bely & J. B. Breckinridge (Bellingham, WA: SPIE), 234
Franceschini, A., Aussel, H., Cesarsky, C. J., Elbaz, D., & Fadda, D. 2001, A&A, 378, 1
Franx, M., et al. 2003, ApJ, 587, L79
Girardi, L., Bressan, A., Chiosi, C., Bertelli, G., & Nasi, E. 1996, A&AS, 117, 113
Glasser, G. J. 1962, J. Am. Stat. Assoc., 57, 648
Greve, T. R., et al. 2005, MNRAS, 359, 1165
Holland, W. S., et al. 1999, MNRAS, 303, 659
Hopkins, P. F., Hernquist, L., Cox, T. J., & Keres, D. 2008, ApJS, 175, 356

Houck, J. R., et al. 2004, ApJS, 154, 18
Houck, J. R., et al. 2005, ApJ, 622, L105
Hughes, D. H., Dunlop, J. S., & Rawlings, S. 1997, MNRAS, 289, 766
Jonsson, P., Cox, T. J., Primack, J. R., & Somerville, R. S. 2006, ApJ, 637, 255
Kenter, A., et al. 2005, ApJS, 161, 9
Koekemoer, A. M., Fruchter, A. S., Hook, R. N., & Hack, W. 2002, in *HST* Calibr. Workshop, Hubble after the Installation of the ACS and the NICMOS Cooling System, ed. S. Arribas, A. Koekemoer, & B. Whitmore (Baltimore, MD: STScI), 337
Krist, J. E., & Hook, R. N. 1997, in the 1997 *HST* Calilor Workshop with a New Generation of Instruments, ed. S. Casertano (Baltimore: STScI), 192
Labbé, I., et al. 2003, AJ, 125, 1107
Law, D. R., Steidel, C. C., Erb, D. K., Larkin, J. E., Pettini, M., Shapley, A. E., & Wright, S. A. 2007, ApJ, 669, 929
Le Floc'h, E., et al. 2005, ApJ, 632, 169
Lotz, J. M., Jonsson, P., Cox, T. J., & Primack, J. R. 2008, MNRAS, 391, 1137
Lotz, J. M., Madau, P., Giavalisco, M., Primack, J., & Ferguson, H. C. 2006, ApJ, 636, 592
Lotz, J. M., Primack, J., & Madau, P. 2004, AJ, 128, 163
Madau, P., Ferguson, H. C., Dickinson, M. E., Giavalisco, M., Steidel, C. C., & Fruchter, A. 1996, MNRAS, 283, 1388
McLaughlin, H., & Wiklind, T., et al. 2007, NICMOS Data Handbook, Version 7.0 (Baltimore, MD: STScI)
Melbourne, J., et al. 2008, AJ, 136, 1110
Mobasher, B. 2002, User's Guide, *Hubble Space Telescope* (Baltimore, MD: STScI)
Murphy, T. W., Jr., Armus, L., Matthews, K., Soifer, B. T., Mazzarella, J. M., Shupe, D. L., Strauss, M. A., & Neugebauer, G. 1996, AJ, 111, 1025
Murray, S. S., et al. 2005, ApJS, 161, 1
Novak, G. S., Cox, T. J., Primack, J. R., Jonsson, P., & Dekel, A. 2006, ApJ, 646, L9
Oke, J. B., et al. 1995, PASP, 107, 375
Papovich, C., Dickinson, M., & Ferguson, H. C. 2001, ApJ, 559, 620
Pavlovsky, C., et al. 2005, ACS Data Handlbook, Version 4.0 (Baltimore, MD: STScI)
Peng, C. Y., Ho, L. C., Impey, C. D., & Rix, H.-W. 2002, AJ, 124, 266
Pérez-González, P. G., et al. 2005, ApJ, 630, 82
Polletta, M., Weedman, D., Hönig, S., Lonsdale, C. J., Smith, H. E., & Houck, J. 2008, ApJ, 675, 960
Pope, A., Borys, C., Scott, D., Conselice, C., Dickinson, M., & Mobasher, B. 2005, MNRAS, 358, 149
Pope, A., et al. 2008, ApJ, 689, 127
Ravindranath, S., et al. 2006, ApJ, 652, 963
Rieke, G. H., et al. 2004, ApJS, 154, 25
Sanders, D. B., Soifer, B. T., Elias, J. H., Madore, B. F., Matthews, K., Neugebauer, G., & Scoville, N. Z. 1988a, ApJ, 325, 74
Sanders, D. B., Soifer, B. T., Elias, J. H., Neugebauer, G., & Matthews, K. 1988b, ApJ, 328, L35
Schade, D., Lilly, S. J., Crampton, D., Hammer, F., Le Fevre, O., & Tresse, L. 1995, ApJ, 451, L1+
Sérsic, J. L. 1968, Atlas de Galaxias Australes, (Cordoba, Argentina: Obs. Astron.)
Soifer, B. T., Sanders, D. B., Neugebauer, G., Danielson, G. E., Lonsdale, C. J., Madore, B. F., & Persson, S. E. 1986, ApJ, 303, L41
Steidel, C. C., Giavalisco, M., Pettini, M., Dickinson, M., & Adelberger, K. L. 1996, ApJ, 462, L17
Tacconi, L. J., et al. 2006, ApJ, 640, 228
Tacconi, L. J., et al. 2008, ApJ, 680, 246
Toft, S., et al. 2007, ApJ, 671, 285
Trauger, J. T., et al. 1994, ApJ, 435, L3
Weedman, D., et al. 2006a, ApJ, 653, 101
Weedman, D. W., et al. 2006b, ApJ, 651, 101
Wilson, C. D., et al. 2008, ApJS, 178, 189
Yan, L., et al. 2004, ApJS, 154, 60
Zirm, A. W., et al. 2007, ApJ, 656, 66